Hydrothermal seepage patterns above a buried basement ridge, eastern flank of the Juan de Fuca Ridge

G. A. Spinelli,[1,2] L. Zühlsdorff,[3] A. T. Fisher,[1] C. G. Wheat,[4] M. Mottl,[5] V. Spieß,[3] and E. R. Giambalvo[6]

Received 27 February 2003; revised 12 September 2003; accepted 29 September 2003; published 14 January 2004.

[1] We use the distributions of sediment physical properties and modeled basement overpressures to estimate the spatial distribution of fluid seepage through sediments over and around the "First Ridge," a buried basement ridge on the eastern flank of Juan de Fuca Ridge. Fluid discharge rates differ by 1 order of magnitude because of differences in sediment hydraulic properties and by 2 orders of magnitude resulting from differences in sediment thickness and basement overpressure. Sediment type distribution appears to have resulted from differences in local seafloor relief. Compression index (ease of consolidation) increases with proportion of hemipelagic material, from 0.5 at 30% hemipelagic to 1.4 at 95% hemipelagic. Permeability at 50% porosity decreases with proportion of hemipelagic material, from 2×10^{-16} m^2 at 30% hemipelagic to 6×10^{-18} m^2 at 95% hemipelagic. Modeled seepage rates, derived from basement overpressures and sediment physical properties, range from 0 to 27 mm/yr. The average seepage rate over the entire 11 km of ridge within our study area is 1.3 mm/yr. On the basis of the model results, half of the total volume flux of seepage from the First Ridge is contributed from 25% of the study area, with flow rates $\geq$1.1 mm/yr. Low seismic reflection amplitude anomalies are generally correlated with areas of high seepage rates. *INDEX TERMS:* 1815 Hydrology: Erosion and sedimentation; 1832 Hydrology: Groundwater transport; 3015 Marine Geology and Geophysics: Heat flow (benthic) and hydrothermal processes; 3022 Marine Geology and Geophysics: Marine sediments—processes and transport; 3025 Marine Geology and Geophysics: Marine seismics (0935); *KEYWORDS:* marine hydrogeology, fluid flux, sediment properties

Citation: Spinelli, G. A., L. Zühlsdorff, A. T. Fisher, C. G. Wheat, M. Mottl, V. Spieß, and E. R. Giambalvo (2004), Hydrothermal seepage patterns above a buried basement ridge, eastern flank of the Juan de Fuca Ridge, *J. Geophys. Res.*, *109*, B01102, doi:10.1029/2003JB002476.

1. Introduction

[2] Seawater circulates through oceanic crust on the axes and flanks of mid-ocean ridges, influencing ocean chemistry [*Mottl and Wheat*, 1994; *Elderfield and Schultz*, 1996] and crustal evolution [*Lister*, 1972; *Sclater et al.*, 1980; *Alt et al.*, 1986; *Jacobson*, 1992]. At mid-ocean ridge axes, where magmatic heat flow is high and sediment cover is low, fluid can be discharged from the crust at hot springs with temperatures greater than 350°C and at velocities on the order of 10^{10} mm/yr [e.g., *Ginster et al.*, 1994]. On mid-ocean ridge flanks, where young, hot crust is partially covered with sediment, fluid is discharged through sediments at temperatures typically less than 65°C and with velocities ranging from <1 mm/yr [e.g., *Wheat and Mottl*, 2000] to 10^{10} mm/yr (C. G. Wheat et al., Heat flow from a basaltic outcrop on a ridge flank: Insights to the role of outcrops in guiding hydrothermal discharge, submitted to *Earth and Planetary Science Letters*, 2003). Most of the convective heat loss from oceanic crust occurs on mid-ocean ridge flanks [*Sclater et al.*, 1980; *Stein and Stein*, 1994]. This large heat flux on ridge flanks at low temperatures relative to ridge axes, requires that approximately 100 times more fluid circulates through ridge flanks than ridge axes [*Mottl and Wheat*, 1994].

[3] Sediment blanketing the crust on mid-ocean ridge flanks controls the communication between fluid within the crust and the oceans [*McDuff*, 1981; *Karato and Becker*, 1983; *Fisher et al.*, 1994; *Snelgrove and Forster*, 1996; *Giambalvo et al.*, 2000]. The degree of coupling between the crustal (basement) aquifer and the ocean affects ocean chemistry [*Mottl and Wheat*, 1994], the transition from advective to conductive heat flow [*Anderson and Hobart*, 1976; *Sclater et al.*, 1976; *Stein and Stein*, 1994], and the nature of hydrothermal alteration of the crust [*Alt and*

[1]Earth Sciences Department, University of California, Santa Cruz, California, USA.
[2]Now at Earth and Environmental Science Department, New Mexico Institute of Mining and Technology, Socorro, New Mexico, USA.
[3]Department of Geosciences, University of Bremen, Bremen, Germany.
[4]Global Undersea Research Unit, University of Alaska Fairbanks, Fairbanks, Alaska, USA.
[5]Department of Oceanography, University of Hawaii, Hawaii, USA.
[6]Sandia National Laboratories, Carlsbad, New Mexico, USA.

0148-0227/04/2003JB002476$09.00

Teagle, 1999]. Point measurements of fluid seepage derived from sediment pore water chemistry profiles have defined narrow seepage zones over basement highs [*Mottl and Wheat*, 1994] on the Juan de Fuca Ridge flank [*Wheat and Mottl*, 1994; *Shipboard Scientific Party*, 1997a; *Mottl et al.*, 1998] and on other margins (e.g., Costa Rica Rift [*Langseth et al.*, 1988; *Mottl*, 1989], Galapagos Rift [*Maris and Bender*, 1982; *Maris et al.*, 1984], and Mariana Trough [*Wheat and McDuff*, 1995]). Some of these focused seepage zones have been attributed to flow along faults [*Williams et al.*, 1979; *Johnson et al.*, 1993; *Mottl et al.*, 1998]. In this study, we determine the degree to which the distribution of sediment (thickness and type) can lead to local spatial variability in fluid discharge rate from a major buried basement ridge in young crust on the sedimented eastern flank of the Juan de Fuca Ridge. Analysis of sediments from a transect of Ocean Drilling Program (ODP) sites across the basement ridge of interest for this study indicates that sediments overlying the basement ridge have higher porosity and permeability than sediments off the ridge, enhancing and potentially focusing seepage over the basement ridge [*Giambalvo et al.*, 2000]. We integrate estimates of basement fluid overpressure and sediment hydraulic properties to generate a spatially continuous map of fluid seepage patterns.

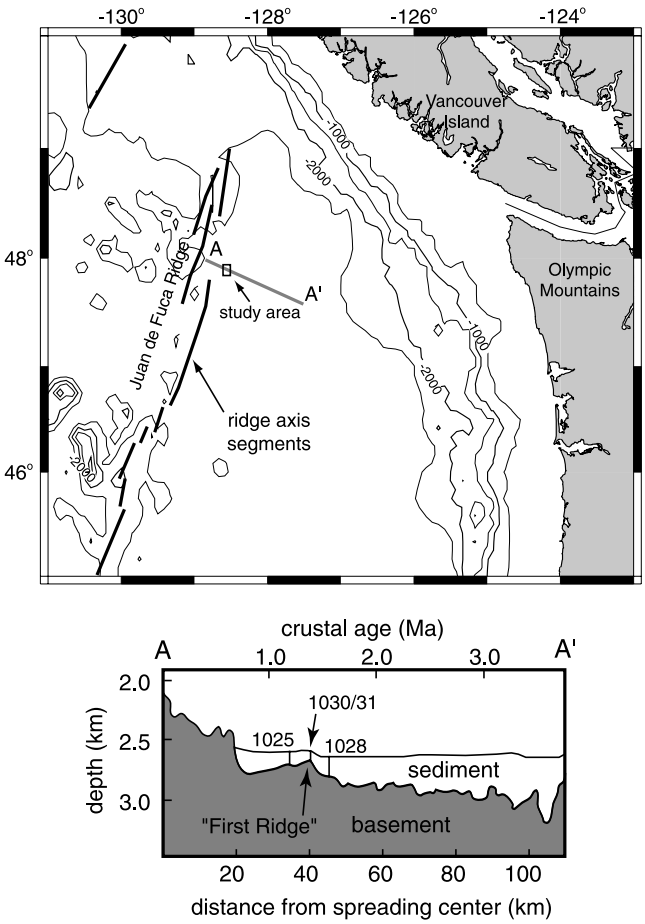

Figure 1. Eastern flank of the Juan de Fuca Ridge. Sediment cores and reflection seismic data were collected on and around the "First Ridge," a sediment covered basement ridge of 1.4 Ma crust. Ocean Drilling Program (ODP) Sites 1030 and 1031 overlie the First Ridge.

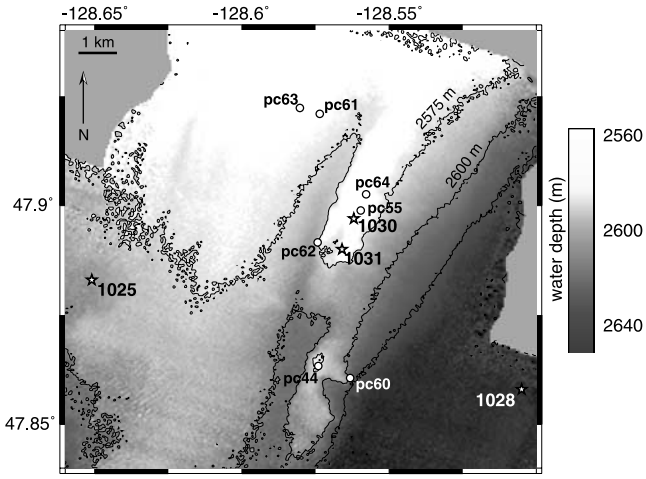

Figure 2. Bathymetry of the First Ridge on the eastern flank of the Juan de Fuca Ridge. The First Ridge plunges to the south. Piston cores (open circles) were collected from on and near the First Ridge in order to analyze the sediments and sediment pore waters. ODP Sites 1030 and 1031 overlie the First Ridge; Sites 1025 and 1028 are ~5 km off the First Ridge.

2. Setting

[4] Our study area is centered on a sedimented basement ridge on the eastern flank of the Juan de Fuca Ridge, approximately 310 km west of the Olympic Peninsula, Washington (Figure 1). Sediment onlaps 0.6 Ma basaltic crust approximately 20 km east of the ridge axis. We focus on and around the "First Ridge," a 1.4 Ma, partially buried, linear basement hill that rises 100–200 m above the surrounding basement and trends NNE-SSW (roughly parallel to the spreading ridge 40 km to the west). The First Ridge is one of a series of parallel ridges likely produced by normal faulting and temporally variable volcanic supply at the ridge axis [e.g., *Kappel and Ryan*, 1986]. ODP Sites 1030 and 1031 overlie the First Ridge; Sites 1025 and 1028 are located approximately 5 km west and east of the First Ridge, respectively. In the southern part of the study area (south of Site 1031) the seafloor overlying the ridge generally rises ~50 m above the surround basins. Proceeding NNE along the axis of the First Ridge from Sites 1031 and 1030, seafloor topography becomes progressively more subdued as the ridge on the seafloor does not rise as high above the surrounding basins (Figure 2). Basement topography is more complex than the bathymetry overlying the First Ridge.

[5] The sediments surrounding the First Ridge are up to 300 m thick; overlying the ridge, the sediment column thins to <40 m. Sandy turbidites up to 1 m thick are found at sites off of the basement ridge. At the ODP sites overlying the crest of the First Ridge, sediments are predominantly hemipelagic mud, with a few fine-grained (silty) turbidite layers [*Shipboard Scientific Party*, 1997b]. The sandy turbidites are sourced from the north and east, with sand potentially

contributed from Vancouver Island, the Olympic Peninsula, and the Fraser River [*Underwood and Hoke*, 2000; M. B. Underwood et al., Provenance, stratigraphic architecture, and hydrogeologic effects of turbidites in northwestern Cascadia Basin, Pacific Ocean, submitted to *Journal of Sedimentary Research*, 2002, hereinafter referred to as Underwood et al., submitted manuscript, 2002]. This is consistent with the distribution of inferred turbidite channels that enter this region from the north, including a channel along the western edge of the First Ridge [*Shipboard Scientific Party*, 1997c; *Zühlsdorff and Spieß*, 2001]. The hemipelagic muds likely have a detrital source similar to the sand [*Underwood and Hoke*, 2000; Underwood et al., submitted manuscript, 2002].

3. Approach for Determining Seepage Distribution

[6] In order to estimate the spatial variability in fluid seepage rate on and around the First Ridge, we develop spatially continuous estimates of fluid overpressure in the basement aquifer (the driving force) and the hydraulic impedance of the sediment column (resistance to flow). The distribution of basement fluid overpressure (pressure above hydrostatic for the ambient, temperature-dependent fluid density) is derived from the calculated overpressure at ODP Site 1031 and the modeled relationship between overpressure and basement relief [*Stein and Fisher*, 2003]. The distribution of sediment hydraulic impedance is derived from the spatial distribution of sediment thickness and type and the relationships between sediment type and geotechnical properties (permeability and consolidation). We focus on the distribution and properties of the fine-grained sediments (hemipelagic muds and silty turbidites) because they have much lower permeabilities than the sandy turbidites [*Giambalvo et al.*, 2000], and so will dominate the seepage pattern. We compare our spatially continuous estimate of fluid discharge with seepage rates determined from pore water chemistry profiles at 17 locations on and around the First Ridge [*Wheat and Mottl*, 1994; *Giambalvo et al.*, 2002; this study].

4. Methods

4.1. Seafloor and Basement Topography

[7] Basement topography (used to estimate the fluid overpressure in basement) and sediment thickness (necessary to determine the hydraulic impedance of sediment columns) are determined from bathymetric maps and closely spaced high-resolution reflection seismic data. A detailed bathymetric map of the First Ridge area was generated with a Hydrosweep multibeam swath sounder. The Hydrosweep system was hull mounted and was heave, roll, and pitch compensated. We interpreted a set of high-resolution multichannel seismic data in order to map basement elevation and sediment thickness over and around the First Ridge. The seismic source was a GI-Gun (2 × 0.4 L), with a frequency range of 100–500 Hz, and shot rate of ~10 s. Data were recorded in 48 channels, received with a 600 m long streamer plus a 100 m long stretch section. Details of the multichannel seismic data acquisition and processing are available from *Zühlsdorff and Spieß* [2001]. Finally, a 4 kHz Parasound echo sounder provided high-resolution images of the upper 50–100 m of the sediment column.

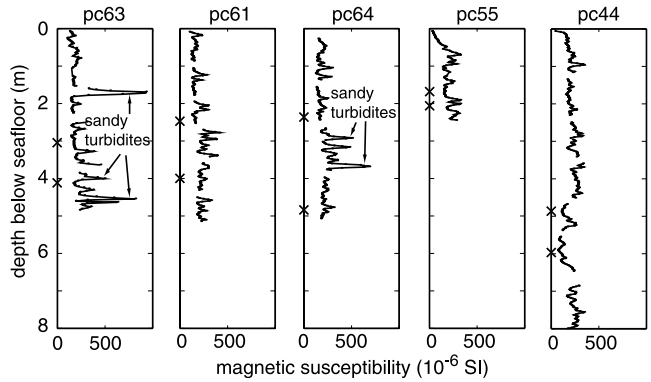

Figure 3. Magnetic susceptibility of sediments from piston cores. Peaks in magnetic susceptibility correspond to sandy turbidites; fine-grained sediments have low magnetic susceptibility. Two samples were selected from each core for permeability and consolidation measurements; sample locations are indicated with a cross along the *y* axis for each core. Sediments were also tested from two additional cores (for which magnetic susceptibility data were not collected).

4.2. Sediment Physical Properties

[8] Sediments from seven conventional piston cores (3–8 m long) and from nearby Ocean Drilling Program Sites 1025, 1028, 1030, and 1031 are used to determine the distribution of sediment types. Five of the seven piston cores overlie the First Ridge; two northern cores are located approximately 1.5 km off of the ridge (Figure 2). Physical properties were measured continuously on five of the piston cores with a multisensor track. Grain size distributions of 48 sediment samples are used to differentiate sediment types. The grain size samples were sieved to separate the sand ($\geq$63 μm) fraction. We determine the distribution of silt and clay sized particles with an X-ray sedigraph. We determine consolidation properties and permeability of 14 fine-grained sediment samples, two from each of the seven cores (Figure 3). We performed one-dimensional consolidation tests with a back-pressured, fixed-ring consolidation cell [*Rowe and Barden*, 1966]. Vertical permeability measurements were made using the steady state flow pump method [*Olsen et al.*, 1985] with low-gradient flows induced at multiple rates, in both directions, through the samples at each consolidation step.

4.3. Pore Water Chemistry

[9] We determine the seepage rates at the locations of the seven sediment cores analyzed for sediment physical properties by fitting solutions of a 1-D advection-diffusion equation to pore water chemistry profiles. The lower limit of fluid seepage rate that can be detected by deviations in pore water magnesium concentration varies with sediment thickness [*Spinelli et al.*, 2004]; it ranges from <0.1 mm/yr for a 50 m thick sediment column to ~0.02 mm/yr for a 200 m thick sediment column. Point measurements of seepage rates are compared to the spatially continuous estimates of fluid seepage rate that we develop.

[10] Pore water magnesium concentrations were determined by titration [e.g., *Wheat and Mottl*, 1994, 2000]. We calculate the concentration of magnesium in sediment pore water as a result of advection and diffusion with temporally variable ocean bottom water chemistry. As noted by *Wheat and Mottl* [1994], the pore water magnesium concentrations on portions of the Juan de Fuca Ridge flank with no fluid flow follow diffusive profiles, indicating that sediment-seawater reactions do not alter magnesium concentrations in this setting. Therefore, for vertical fluid flow, temporal changes in the concentrations of magnesium are described by diffusion and advection [*Berner*, 1980]:

$$\frac{dc}{dt} = \frac{1}{\phi}\left[\frac{d}{dz}\left(\phi D_s \frac{dc}{dz}\right)\right] - v\frac{dc}{dz} \tag{1}$$

where z is depth below seafloor, ϕ is porosity, D_s is the diffusion coefficient in sediment, and v is the average linear fluid velocity relative to the seafloor (negative for upflow). We assume porosity at a given depth below the seafloor does not change with time (i.e., there is steady state sediment accumulation [*Berner*, 1980]). We do account for the decrease in sediment porosity with depth. The effect of mechanical dispersion is assumed to be insignificant, given the small fluid seepage velocities (on the order of 1 mm/yr) through these low-permeability sediments. The diffusion coefficient in sediment is defined as [*Ullman and Aller*, 1982]

$$D_s = \frac{D_w}{\phi F} \tag{2}$$

where D_w is the diffusion coefficient for magnesium in water [*Li and Gregory*, 1974] and F is sediment formation factor. The diffusion coefficients are temperature dependent [*Li and Gregory*, 1974]. We apply a linear temperature increase with depth, from 3°C at the seafloor to 40°C at the sediment-basement interface, based on temperatures at ODP Sites 1030 and 1031 [*Shipboard Scientific Party*, 1997b]. Linear temperature profiles are acceptable, as the temperature profiles are mainly conductive for flow rates up to 300 mm/yr [*Giambalvo et al.*, 2002] and the increase in sediment thermal conductivity due to the decrease in porosity with depth is small. Sediment porosity decreases with depth; results from sediment consolidation experiments (see below) are used to model sediment porosity as a function of depth below the seafloor. We use the formation factor versus depth relationship derived for ODP Site 1030, which is dominated by hemipelagic sediment [*Shipboard Scientific Party*, 1997b]

$$F = 2.96z^{0.015} \tag{3}$$

in calculating D_s.

[11] The fluid velocity through the sediment (v), with respect to the seafloor, results from both a pressure gradient due to basement fluid overpressure and the effects of sediment accumulation and compaction. We will ultimately compare modeled fluid upflow speeds determined from basement fluid overpressure and sediment hydraulic impedance to the seepage rates derived from pore water chemistry profiles. In order to separate the fluid velocity due to basement overpressure from the fluid velocity due to sedimentation and compaction, we include the effects of sediment accumulation and compaction in our calculations of magnesium concentrations. For these calculations we assume steady state compaction (i.e., constant sediment accumulation rate and constant sediment type). For steady state compaction the porosity of sediment at any given depth below the seafloor is constant. With the addition of sediment at the seafloor, the sediment column lengthens and the porosity of sediment at the sediment-basement interface is decreased. At any point in the sediment column, fluid velocity due to compaction (with respect to the seafloor) is calculated from the porosity versus depth profile using [*Berner*, 1980]

$$v_{\text{compaction}} = \frac{\phi_{\text{bot}}}{\phi} w_{\text{bot}} \tag{4}$$

where ϕ_{bot} is sediment porosity at the sediment-basement interface and w_{bot} is the burial rate of sediment at the sediment-basement interface (a function of both sediment accumulation at the seafloor and compaction of the sediment column). We use a sediment accumulation rate of 0.07 mm/yr, based on the average sediment accumulation rates at ODP Sites 1030 and 1031 [*Shipboard Scientific Party*, 1997b]. We calculate the fluid velocity due to sedimentation/compaction with depth and include it in the average linear fluid velocity term, v. The net effect of steady state sediment accumulation and compaction on the fluid seepage velocity with respect to the seafloor is fluid downflow at a speed less than the sediment accumulation rate. From the reference frame of the seafloor, sediment accumulation with no compaction moves pore water down at the sediment accumulation rate (i.e., it is stationary relative to the basaltic basement). Steady state compaction of the sediment column moves the seafloor down at a rate which is a fraction of the sedimentation rate. So, the fluid velocity due to sedimentation/compaction is small (<0.07 mm/yr) and directed downward. As a result, the fluid upflow speeds due to basement fluid overpressure will be slightly (<0.07 mm/yr) larger than if sediment accumulation and compaction were not considered.

[12] The sediment-basement interface is a constant concentration boundary, with the magnesium concentration fixed at the Site 1030 and 1031 basement value, 5.2 mmol/kg [*Shipboard Scientific Party*, 1997b]. Magnesium concentration at the seafloor varies temporally between interglacial and glacial (concentrations ~4% higher than present) values [*Imbrie et al.*, 1984]. Initial pore water magnesium concentrations are determined by analytical solutions describing advection and diffusion between two constant concentration boundaries. For each sediment core, we find the average linear fluid velocity that minimizes the misfit between modeled and measured magnesium concentrations (Figure 4).

5. Sediment Distribution and Type

5.1. Grain Size Distributions

[13] Grain size distributions are used to differentiate sediment types. The fine-grained sediments are our primary

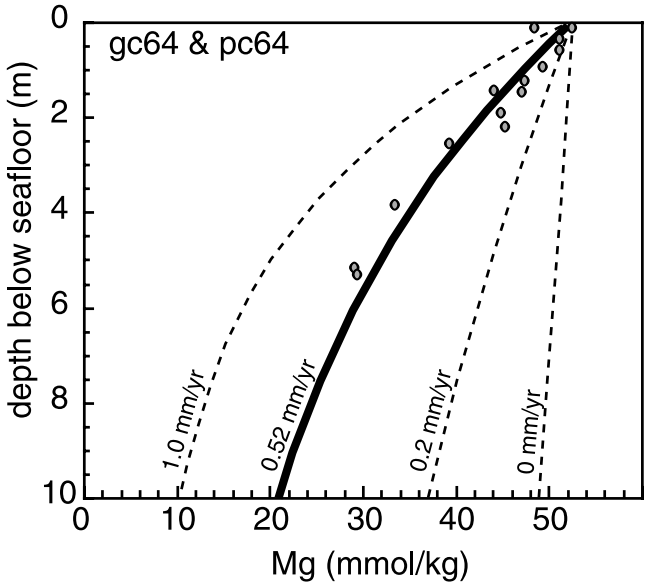

Figure 4. Example of modeling fluid flow rate from pore water chemistry. Circles show Mg concentration in pore waters from a gravity core and piston core. Lines are modeled Mg concentrations using an advection-diffusion equation. The best fit between modeled and observed Mg concentrations (solid line) occurs with an upflow rate of 0.52 mm/yr. Modeled Mg concentrations with upflow rates of 0, 0.2, and 1.0 mm/yr (dashed lines) are shown for comparison.

concern, as they have relatively low permeability and therefore largely determine the effective permeability of the entire sediment column. Of the 48 samples analyzed, 23 were selected from the finest grained (i.e., low magnetic susceptibility) sections of the sediment cores (Figure 3). Fine-grained turbidites have larger median grain size (median 2.7 μm; $n = 12$) and broader grain size distributions (interquartile range 7.3 μm) than do hemipelagic sediments (median 1.9 μm, interquartile range 3.7 μm, $n = 11$). Both the differences in median grain size and interquartile range between fine-grained turbidites and hemipelagic sediments are significant to the 99% level.

[14] Differences in grain size distributions corresponding to sediment type are used to place each sediment sample on a continuum between lithologic end-members. End-member grain size distributions are defined such that the sample grain size distributions can be described as a linear combination of the end-member distributions [*Weltje*, 1997; *Prins and Weltje*, 1999]. Linear combinations of three end-member grain size distributions can describe more than 95% of the variability of the sample grain size distributions. The three end-members are sandy turbidite, fine-grained turbidite, and hemipelagic sediment (Figure 5). The fine-grained samples are generally a combination of fine-grained turbidite and hemipelagic end-members (Figure 6). Two samples between the hemipelagic and sandy turbidite end-members are hemipelagic samples with relatively large numbers of foraminifera (>63 μm). Although the relatively high sand sized fraction in these samples is clearly not turbiditic in origin, the grain size distribution modeling is insensitive to sediment composition. Fine-grained samples range from 27% to 94% hemipelagic (Table 1). Samples for each grain size distribution were collected from ~2 cm long sections of the cores. The proportion of fine-grained turbidite in each fine-grained sample (i.e., its position along the continuum between fine-grained turbidite and hemipelagic end-members) may reflect the number and thickness of thin fine-grained turbidite layers within the ~2 cm long section of core sampled.

5.2. Spatial Distribution of Sediment Types

[15] We model the lateral distribution of sediment types (proportions of fine-grained turbidite and hemipelagic sediment) in order to estimate the sediment permeability (and

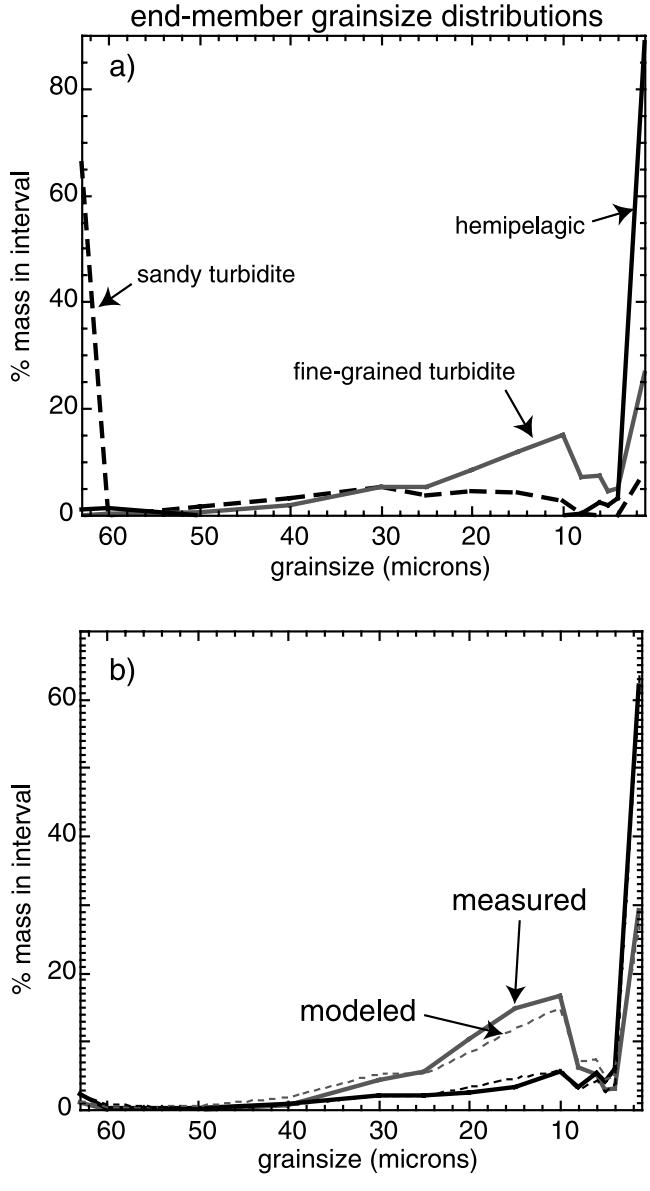

Figure 5. End-member modeling of grain size distributions. (a) Three theoretical end-member grain size distributions are used to model >95% of the variability in grain size distributions. (b) Comparisons between typical observed grain size distributions (solid lines) and modeled distributions (dashed lines) which are linear combinations of the end-members shown in Figure 5a.

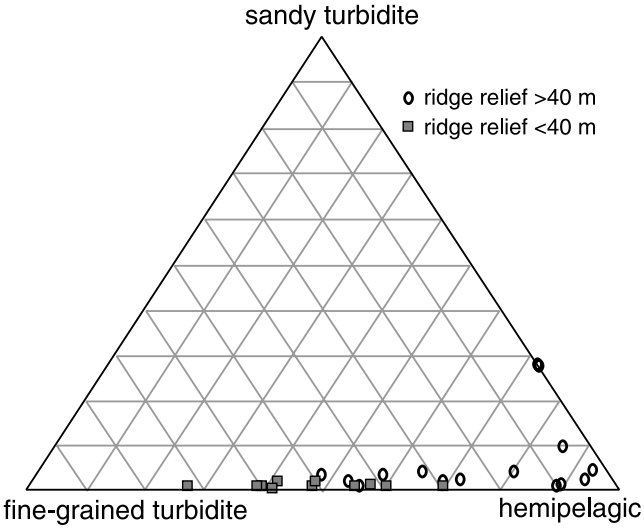

Figure 6. Composition of fine-grained sediment samples based on end-member analysis of grain size distributions. Sediments overlying the First Ridge south of Site 1030, where the local relief between the ridge and the surrounding basins is >40 m (open circles), are more hemipelagic than sediments off the ridge or over the ridge in lower relief areas, north of Site 1030 (solid squares).

hydraulic impedance) on and around the First Ridge. The topography of the First Ridge affects the pattern of turbidite deposition in the area. First, we describe the observed spatial variation in sediment types. Then, we discuss the degree to which topography on the scale of the First Ridge could impact turbidite deposition. Finally, we model the distribution of sediment types based on spatial trends.

[16] Sediments from Site 1031, overlying the crest of the First Ridge, are predominantly hemipelagic mud, with a few fine-grained turbidite layers. The sediments at Site 1030, approximately 1 km north of Site 1031, are also predominantly hemipelagic mud, but fine-grained turbidites are more abundant at Site 1030 than at Site 1031 [*Shipboard Scientific Party*, 1997b]. No sandy turbidites were recovered at Sites 1030 or 1031 [*Shipboard Scientific Party*, 1997b]. Overlying the ridge approximately 600 m farther north, a few thin (<0.1 m) sandy turbidites are found in the upper 5 m of sediment. In the basins surrounding the First Ridge, at ODP Sites 1025 and 1028, sandy turbidites are up to 1 m thick.

[17] An earlier study demonstrated that the fine-grained sediments from ODP Sites 1030 and 1031 (overlying the First Ridge) are more hemipelagic than fine-grained sediments from ODP sites off of the basement ridge [*Giambalvo et al.*, 2000]. Hemipelagic sediments in this area have abundant foraminifera (1–5 vol %; and >10 wt % carbonate content), randomly oriented clays, and a high compression index (ease of consolidation). Fine-grained turbidites have few or no foraminifera, well laminated clays, and a low compression index [*Giambalvo et al.*, 2000]. On the basis of end-member modeling of grain size distributions, fine-grained sediments overlying the First Ridge south of Site 1030 are more hemipelagic than either fine-grained sediments overlying the ridge to the north of Site 1030 or sediments off the ridge. Samples overlying the ridge from Site 1030 to the south are 48–94% hemipelagic (mean 73%). Samples over the ridge to the north of ODP Site 1030 and samples off of the First Ridge are 27–70% hemipelagic (mean 48%) (Figure 6). Along the First Ridge, seafloor topography grades from a slightly muted form of the basement topography in the south, rising more than 60 m above the surrounding seafloor, to a relatively flat region in the north, with little relief between the seafloor overlying the basement ridge and adjacent areas (Figure 7). North of Site 1030, where shallow sediments are more turbiditic, the relief between the seafloor overlying the ridge and the surrounding basins is <40 m. South of Site 1030, where shallow sediments are more hemipelagic, local seafloor relief is >50 m.

[18] Turbidite deposition can be dramatically affected by seafloor topography as demonstrated by field observations and laboratory experiments. Evidence from the rock record suggests that seafloor topography can completely block and reflect turbidity currents [*Pickering and Hiscott*, 1985] or it can deflect turbidity currents obliquely [*Haughton*, 1994]. Turbidity current reflection along basin margins is suggested by high angles between inferred flow directions for basal and upper portions of turbidites [e.g., *Kneller et al.*, 1991; *Pickering et al.*, 1992; *Haughton*, 1994].

[19] Sedimentation patterns on and around the First Ridge are clearly affected by turbidity currents interactions with topography. Sandy turbidites, common at sites 5 km east and west of the ridge, are absent at Sites 1030 and 1031 overlying the First Ridge. The ability of the First Ridge to block westward moving turbidity currents is also suggested by the timing of local turbidite deposition (Underwood et al., submitted manuscript, 2002). Turbidite deposition 5 km west of the First Ridge, at Site 1025, begins ~0.45 Myr later than turbidite deposition 5 km east of the ridge, at Site 1028 [*Shipboard Scientific Party*, 1997c; Underwood et al., submitted manuscript, 2002]. The effect seafloor topography has upon a turbidity current is a function of the properties of both the turbidity current (e.g., velocity, thickness, and density stratification) and the topography (e.g., height, slope, and shape). Flume experiments indicate that turbidity currents can be partially deflected by topography with relief on the same order as turbidity current thickness [*Kneller et al.*, 1991; *Alexander and Morris*, 1994; *Haughton*, 1994].

[20] For a turbidity current or surge interacting with complex topography, such as a ridge of finite length or a ridge with gaps, some or all of the flow may be diverted around the topography. The regional, fine-grained, shallow sediment type distribution, dominantly hemipelagic overlying the basement ridge to the south of ODP Site 1030, where seafloor topography is more pronounced, and dominantly turbiditic to the north, may have resulted from differences in local seafloor relief (Figure 7). A continuous ridge 50 m high could block turbidity currents or surges, with typical velocities and suspended sediment concentrations, up to 40 m thick [*Rottman et al.*, 1985; *Middleton*, 1993; *Normark and Piper*, 1991; *Stow*, 1994; *Kneller and McCaffrey*, 1999; *Kneller and Buckee*, 2000]. For flows thicker than local topography, much of the dense lower portion of the flow could be diverted around 3-D topography [*Baines*, 1979; *Snyder et al.*, 1985; *Kneller and McCaffrey*,

Table 1. Grain Size, Magnetic Susceptibility, End-Member Grain Size Modeling Results, and Physical Properties of Juan de Fuca Ridge Flank Sediments

Core	Depth, m	Median Grain Size, μm	Grain Size IQR μm	Magnetic Susceptibility 10^{-6} SI	Percent Sandy Turbidite	Percent Fine Grained Turbidite	Percent Hemipelagic	Permeability at 50% Porosity	Compression Index
pc44	0.96	2.3	7.8	345	0	55	44	-	-
pc44	1.08	3.1	7.8	181	0	65	35	-	-
pc44	1.97	1.9	5.4	177	1	45	54	-	-
pc44	2.85	2.7	7.8	329	0	60	40	-	-
pc44	3.00	1.8	5.3	240	1	44	55	-	-
pc44	3.17	1.4	3.6	166	1	29	70	-	-
pc44	3.60	6.6	18.6	326	6	74	20	-	-
pc44	4.10	2.3	5.1	285	0	50	50	-	-
pc44	4.85	2.4	5.5	111	3	49	48	2.11×10^{-17}	1.03
pc44	5.23	4.3	10.6	257	1	71	28	-	-
pc44	5.95	1.9	4.8	81	2	38	59	1.57×10^{-17}	1.23
pc44	7.56	1.4	3.4	346	1	26	73	-	-
pc55	1.66	2.8	7.2	165	0	60	40	4.30×10^{-17}	0.71
pc55	2.05	2.7	8.4	249	1	57	42	1.33×10^{-16}	0.61
pc60	2.30	1.5	0.8	-	0	10	90	2.19×10^{-17}	0.90
pc60	2.38	1.9	4.5	-	0	44	56	1.48×10^{-17}	1.11
pc61	0.68	1.8	4.5	119	0	41	59	-	-
pc61	1.23	8.4	11.8	279	2	98	1	-	-
pc61	1.60	1.9	4.8	137	0	48	52	-	-
pc61	2.47	1.7	5.0	154	0	45	55	3.05×10^{-17}	0.73
pc61	2.77	5.4	9.2	416	0	84	16	-	-
pc61	2.95	6.9	16.8	380	8	72	20	-	-
pc61	3.38	6.0	9.9	388	0	88	12	-	-
pc61	4.00	4.0	8.6	275	0	73	27	3.75×10^{-16}	0.38
pc61	4.58	4.5	9.1	327	1	74	25	-	-
pc61	4.96	2.7	7.0	179	0	61	39	-	-
pc62	2.35	2.3	7.9	-	0	58	42	3.80×10^{-17}	0.66
pc62	5.00	1.8	3.9	-	3	31	65	4.80×10^{-17}	0.80
pc63	1.41	1.8	4.9	169	0	42	58	-	-
pc63	1.62	10.9	23.3	404	18	74	8	-	-
pc63	1.65	9.2	23.6	553	21	66	13	-	-
pc63	1.69	60.8	36.3	931	100	0	0	-	-
pc63	1.85	1.7	4.6	142	0	39	61	-	-
pc63	2.00	3.8	9.2	236	3	66	31	-	-
pc63	2.66	7.2	16.1	279	5	77	17	-	-
pc63	3.05	0.9	3.5	171	0	30	70	2.36×10^{-17}	0.66
pc63	3.26	8.4	13.7	380	1	95	4	-	-
pc63	4.05	1.8	6.8	215	0	52	48	3.40×10^{-17}	0.57
pc64	2.35	2.5	6.9	165	0	59	41	7.64×10^{-17}	0.74
pc64	4.82	2.4	7.0	204	0	58	42	7.64×10^{-17}	0.51
1028	17.0	2.0	6.9	-	1	51	48	8.72×10^{-17}	0.41
1030	20.0	<0.3	<0.6	-	1	5	94	8.94×10^{-18}	1.27
1030	20.0	0.9	<2.8	-	3	16	81	8.94×10^{-18}	1.27
1030	34.8	2.3	1.1	-	0	9	90	5.48×10^{-18}	1.38
1031	23.2	1.6	7.8	-	27	0	73	1.23×10^{-17}	1.15
1031	23.2	0.6	2.4	-	27	0	73	1.23×10^{-17}	1.15
1031	30.3	0.5	0.5	-	4	2	94	2.51×10^{-18}	1.93
1031	39.2	<0.3	<0.7	-	9	5	86	2.63×10^{-18}	1.17

1999; *Kneller and Buckee*, 2000]. Individual turbidity currents on the eastern flank of the Juan de Fuca Ridge each adjust to the topography encountered on their own flow paths, resulting in complex, patchy turbidite deposition (Underwood et al., submitted manuscript, 2002). The lateral continuity of turbidites around and over topographic highs varies with the size, shape, and slope of the topography and the hydrodynamic properties of the turbidity currents that deposits them.

[21] We model the distribution of sediment types throughout the study area based on spatial trends and relations. Sediment type varies little between the four shallow (<5 m) cores to the north of ODP Site 1030. Sediment type north of Site 1030 does not vary systematically with bathymetry, distance from the First Ridge, sediment thickness, latitude, or longitude. We propose that the wide distribution of fine-grained sediments with a relatively high proportion of fine-grained turbidites (low proportion of hemipelagic sediment) north of Site 1030 may result from turbidity currents being relatively unimpeded by local seafloor relief. Where the relief from the ridge to the surrounding basins is relatively low (<40 m), we model the shallow sediment type as a constant, 45% hemipelagic (mean value for four cores north of Site 1030). South of Site 1030 the local seafloor relief is greater and the proportion of hemipelagic sediment between three piston cores and ODP Sites 1025, 1028, 1031 varies inversely with sediment thickness and distance from the basement ridge (Figure 8). The observed distribution of shallow sediment types, based on our limited number of sediments cores, is consistent with fine-grained sediment

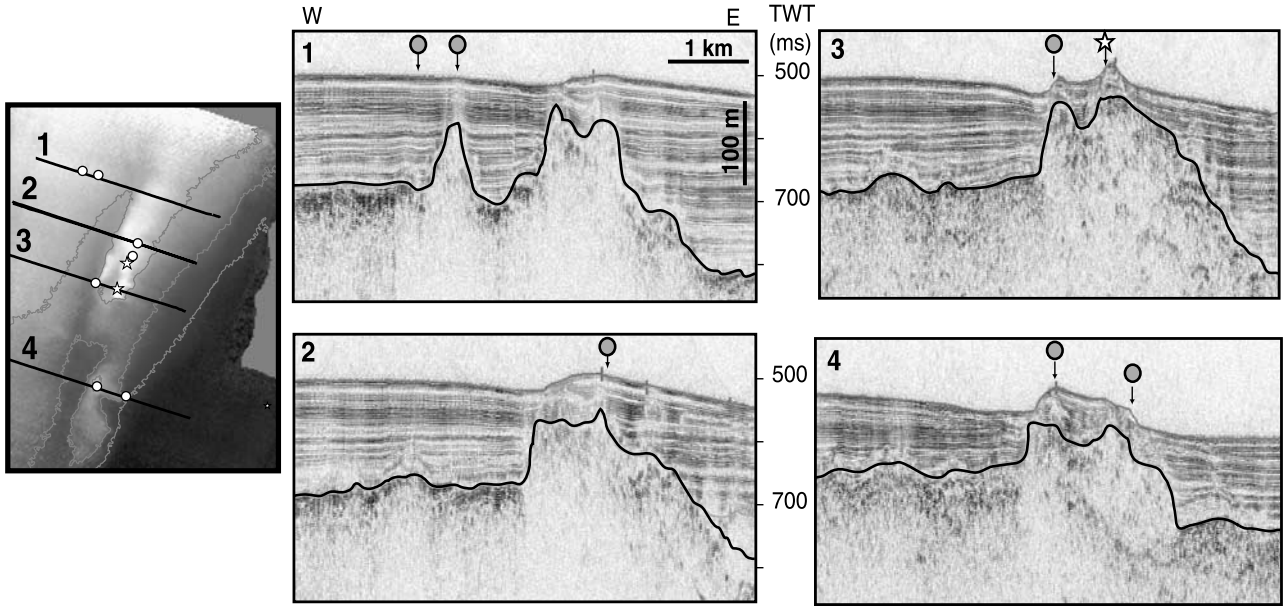

Figure 7. Reflection seismic data along four profiles across the First Ridge. The locations of the seismic lines are indicated on the map to the left. Locations of piston cores (circles) and ODP Site 1031 (stars) are indicated above the reflection seismic profiles. First Ridge topography in the north is subdued, as the basins surrounding the ridge have largely filled with sediment. In the south, First Ridge topography is more pronounced.

accumulation resulting from the interaction of hemipelagic and turbidite sedimentation on and around seafloor topography. The proportion of hemipelagic sediment varying inversely with sediment thickness may result from a relatively constant accumulation of hemipelagic sediment spatially, and increased sediment thickness where more turbidites have accumulated. The decrease in the proportion of hemipelagic sediment (increase in proportion of fine-grained turbidites) with distance from the First Ridge may indicate that turbidity currents are somewhat restricted to the basins surrounding the First Ridge. Where the relief from the ridge to the surrounding basins is greater than 40 m, we model the shallow sediment type as a function of both the sediment thickness and the distance from the First Ridge; the resulting sediment types vary from 35% to 95% hemipelagic material (Figure 9).

5.3. Depth Variations in Sediment Type

[22] The spatial distribution of sediment types based primarily on piston cores (<8 m long) indicates trends in recent sediment accumulation, but may not accurately depict the sediment types at depth. Assuming a linear sedimentation rate from the seafloor to the first nannofossil determined age at the ODP Sites overlying the First Ridge [*Shipboard Scientific Party*, 1997b], Holocene sediments (<10,000 yrs) are confined to the upper ~0.7 m of sediment, and the deepest sediments collected by conventional piston coring are approximately 110,000 yrs old. Therefore sediments from the piston cores record sedimentation over a wide range of climatic and sea level conditions. The range of sediment types and properties determined for samples from the shallow (<8 m) piston cores is consistent with the range of sediments encountered in the entire sedimentary sections at the local ODP sites. This suggests that the range of processes that controlled recent (<110,000 yrs; <8 m depth) sediment accumulation may be similar to the range of processes that acted during earlier (deeper) sediment accumulation.

[23] There is no apparent variation in sediment type with depth at Site 1031; temporal variations in sediment supply, seafloor morphology, or other controlling factors did not significantly affect the style of sediment accumulation (primarily hemipelagic sediment) at this site. At Site 1030 the number of silty turbidites generally decreases with depth (Figure 8c), which is consistent with an increase in the proportion of hemipelagic sediment with depth. This variation in sediment type with depth could result from temporal variability in sediment supply (i.e., the number, thickness, or composition of turbidity currents) and/or the evolution of seafloor topography around the First Ridge. Given our conceptual model of sediment accumulation on and around the First Ridge, sediments overlying the First Ridge to the north of Site 1030 should become more hemipelagic with depth due to the evolution of seafloor topography. Currently, there is little relief between the ridge to the north of Site 1030 and the surrounding basins. However, earlier in the history of the First Ridge, the relief between the ridge in the north and the surrounding basins would have been greater. As the basins surrounding the First Ridge fill with sediment, the influence of topography on turbidity currents is reduced (Underwood et al., submitted manuscript, 2002). This is consistent with the observed increase in the proportion hemipelagic sediment with depth at Site 1030. Additionally, shallow (<5 m) fine-grained sediments from two piston cores slightly north (~200 and 600 m) of Site 1030 are less hemipelagic (more fine-grained turbiditic) than deeper (>20 m) samples from Site 1030 (Figure 8c), and a few thin sandy turbidites are found in the shallow sediments ~600 m north of Site 1030. There are no

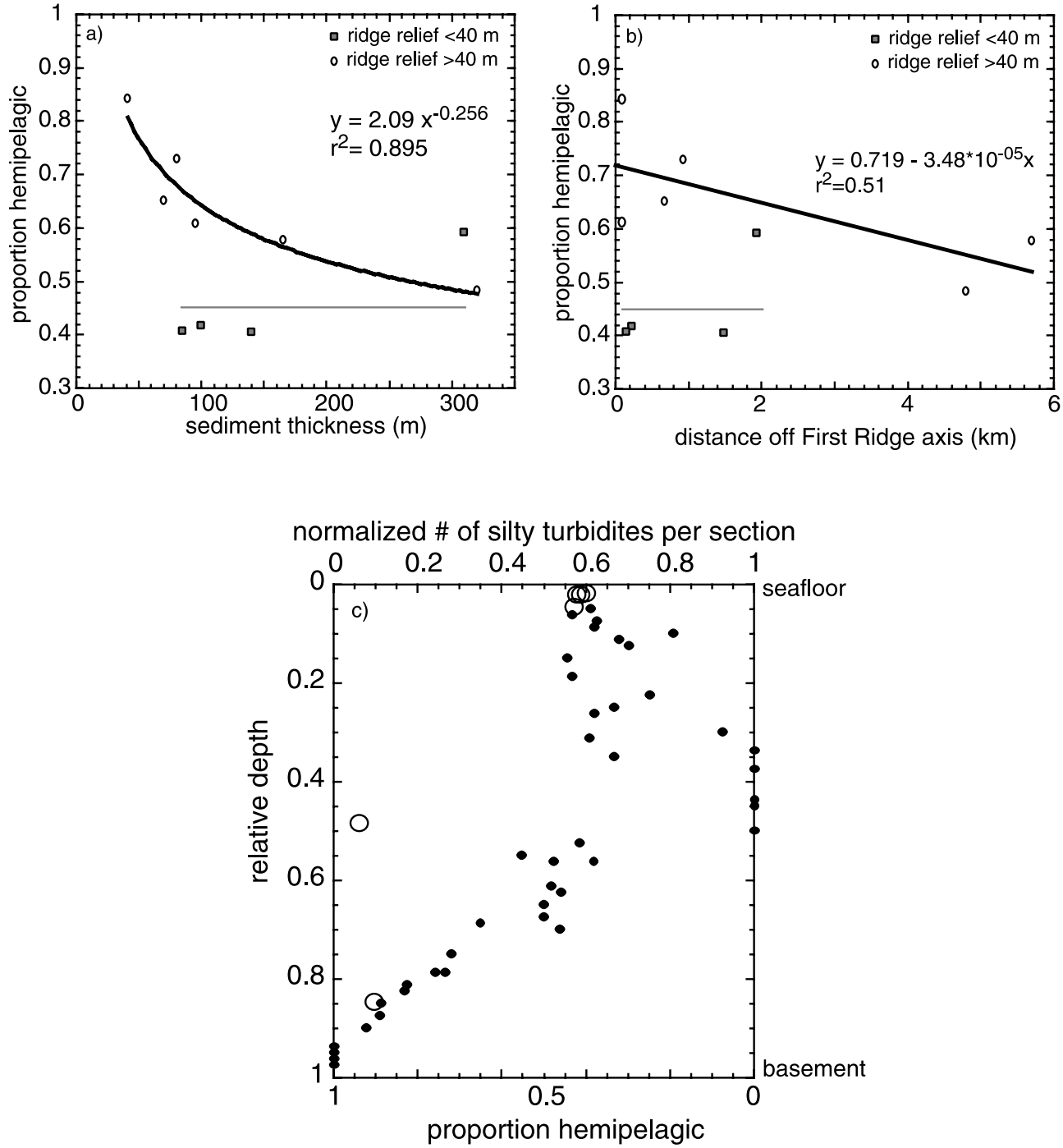

Figure 8. Spatial variation in sediment type on and around the First Ridge. Where ridge relief is more pronounced, the proportion of hemipelagic sediment comprising the sediments decreases with increasing sediment thickness (Figure 8a) and increasing distance from the First Ridge (Figure 8b). The number of fine-grained turbidites (dots; upper axis) at ODP Site 1030 increases to a maximum ~20 m below the seafloor, then decreases sharply in the lower half of the section (Figure 8c). The proportion of hemipelagic sediment comprising fine-grained samples (open circles; lower axis) is relatively low in shallow samples slightly north of Site 1030 and is much higher in deep samples from Site 1030.

sandy turbidites at Site 1030 [*Shipboard Scientific Party*, 1997b]. Sandy turbidites at Sites 1025 and 1028 are confined to the upper 60–70% of the sediment column, but detailed information about depth variations of fine-grained sediments is not available.

[24] We can not rule out temporal variations in sediment supply affecting fine-grained sediment accumulation patterns in the basins off of the First Ridge. However, the combination of data from piston cores and ODP Sites 1030 and 1031 allows us to make some inferences about varia-

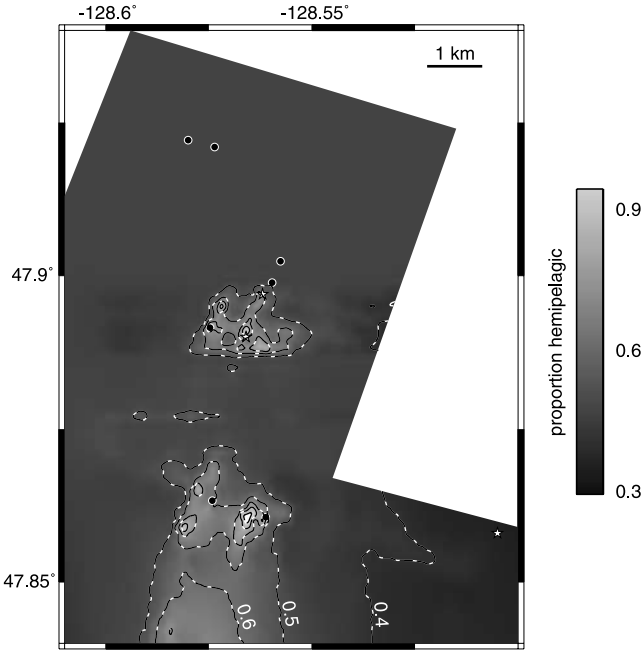

Figure 9. Modeled distribution of shallow sediment types on and around the First Ridge. The proportion of hemipelagic material within sediments overlying the First Ridge ranges from 95% where ridge relief is high (>40 m) and sediments are thin to 45% where ridge relief is low (<40 m). Off of the First Ridge fine-grained sediments are predominantly fine-grained turbidites (<50% hemipelagic).

tions in sediment type with depth overlying the First Ridge. Modeled sediment type increases in proportion hemipelagic sediment with depth overlying the ridge, where local relief is less than 40 m; elsewhere, modeled sediment type is constant with depth.

6. Seepage Rates From Pore Water Chemistry

[25] Fluid seepage rates determined at points on and around the First Ridge provide information on the range of seepage speeds and the distance over which variability in upflow speed occurs. Results of modeling seepage from overpressure and sediment distributions are compared to these point measurements of fluid discharge. Ten point estimates of fluid seepage overlying the First Ridge have been previously determined from pore water chemistry profiles. Seven seepage rates were determined for piston and gravity cores distributed along the First Ridge; fluid upflow estimates from magnesium data range from 0.1 to 2.0 mm/yr [*Wheat and Mottl*, 1994]. These are total fluid seepage rates, combining the effects of basement fluid overpressure and sedimentation/compaction. Although the effects of steady state sediment accumulation and compaction have a minor impact on the modeled fluid seepage rates, we apply a correction to the seepage rates from *Wheat and Mottl* [1994], so all the seepage rates that we compare are due only to basement fluid overpressure. At the seven sites where we calculated seepage rates from pore water chemistry profiles the sediment thickness ranges from 40 to 310 m. At these sites, the fluid downflow (with respect to the seafloor) due to sedimentation/compaction ranges from 0.03 to 0.016 mm/yr, respectively, with an average downflow rate of 0.026 mm/yr. In order to more accurately approximate the fluid upflow rates due only to basement fluid overpressure at the sites analyzed by *Wheat and Mottl* [1994], we increase their seepage rates by 0.026 mm/yr, effectively accounting for sedimentation/compaction. Fluid upflow rates at ODP Sites 1030 and 1031 are 1.9 and 3.2 mm/yr, respectively [*Giambalvo et al.*, 2002]. *Giambalvo et al.* [2002] account for sediment burial, but not sediment compaction. Sediment accumulation has moved the seafloor up ~0.07 mm/yr at these sites, but sediment compaction reduces that upward movement to ~0.026 mm/yr. Therefore we reduce the fluid upflow rates from *Giambalvo et al.* [2002] by 0.044 mm/yr (effect of sediment accumulation and compaction minus effect of accumulation alone). Seepage rates due to basement fluid overpressure for the seven cores analyzed for this study range from 0.06 to 7.0 mm/yr (Table 2).

[26] Previous studies indicated that fluid upflow rates correlate positively with local heat flow measurements [*Davis et al.*, 1992a] and are inversely related to sediment thickness [*Wheat and Mottl*, 1994]. Fluid upflow through the sediments appears to be limited to areas where sediment thickness is <160 m [*Wheat and Mottl*, 1994]. Basement fluids at Sites 1030 and 1031 are more altered than at surrounding sites. This suggests that the source of the fluid discharging from the sediments on and around the First Ridge could be distinct from the overall flow of basement fluid, which recharges at exposed oceanic crust closer to the ridge axis and moves east [*Shipboard Scientific Party*, 1997b].

7. Sediment Physical Properties

7.1. Consolidation and Permeability

[27] Knowledge of sediment consolidation as a function of effective stress and sediment permeability as a function of porosity allows us to model both porosity and permeability with depth in a sediment column [e.g., *Giambalvo et al.*, 2000]. Both our results and a study of deeper sediment samples on and around the First Ridge [*Giambalvo et al.*, 2000] indicate that primarily hemipelagic sediments have higher initial void ratios (volume voids/volume solids) and higher compression indices (slope of virgin consolidation curve) than primarily fine-grained turbiditic sediments (Figure 10a). Consolidation curves of the shallow sediment samples are shifted toward slightly lower void ratios relative to the deeper samples, for both sediment types. At all depths in the sediment column, hemipelagic sediments have lower

Table 2. Fluid Seepage Rates From Pore Water Chemistry (Mg) Modeling

Cores	Latitude	Longitude	Fluid Upflow Rate, mm/yr
gc44, pc44	47.86332°	−128.57411°	0.16
gc55, pc55	47.89890°	−128.55964°	0.39
pc60	47.86000°	−128.56100°	5.0
gc61, pc61	47.92093°	−128.57389°	0.10
gc62	47.89157°	−128.57507°	7.0
pc63	47.92228°	−128.58032°	0.06
gc64, pc64	47.90258°	−128.55781°	0.52

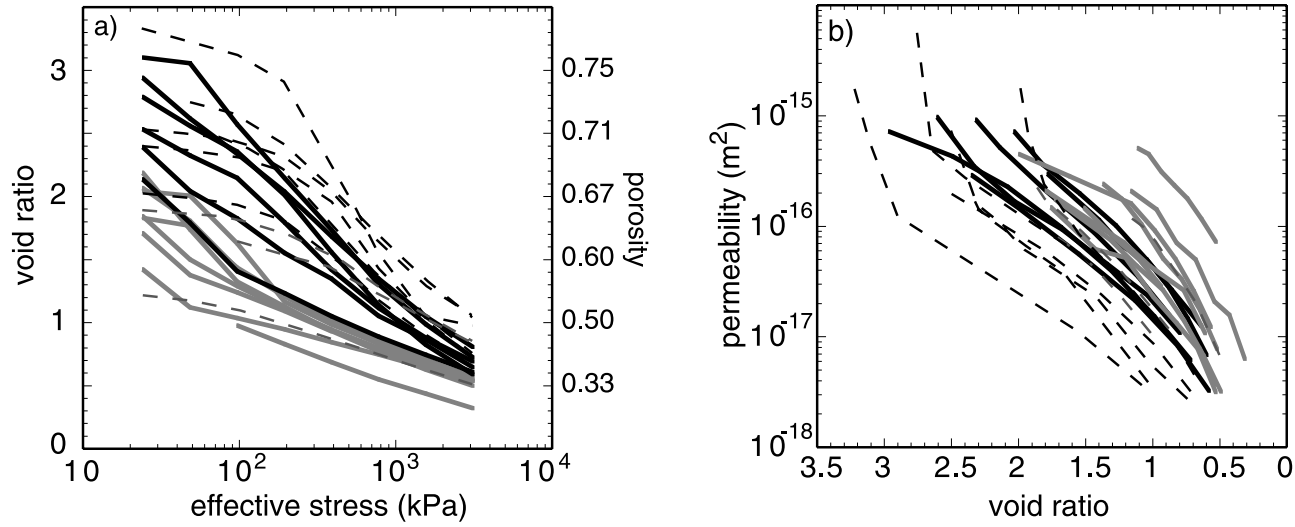

Figure 10. Physical properties of sediments on and around the First Ridge. (a) Both shallow (solid black line) and deep (dashed black line) hemipelagic sediments have higher initial void ratios and consolidate more as they are buried (i.e., increasing effective stress) than either shallow (solid gray line) or deep (dashed gray line) fine-grained turbidites. (b) Hemipelagic sediments (shallow samples, solid black; deep samples, dashed black) have lower permeability at a given void ratio than fine-grained turbidites (shallow samples, solid gray; deep samples, dashed gray). Hemipelagic sediments have higher permeability in the upper 275 m of the sediment column due to their higher porosity.

permeability at a given void ratio than more fine-grained turbiditic sediments (Figure 10b). Similarly, the permeability of shallow sediment is shifted toward slightly lower values than the deeper samples. On the basis of the laboratory determined consolidation and permeability relationships, hemipelagic sediments have higher in situ permeability than fine-grained turbidites in the upper 275 m of the sediment column. Below 275 m the porosity of hemipelagic sediment is reduced sufficiently, such that fine-grained turbidites have higher permeability.

[28] Although there is considerable scatter in the porosity data for ODP Sites 1030 and 1031, we can compare the porosity calculated from consolidation testing results to functions fit to the measured porosity data. Throughout the entire sediment column, the porosity of the hemipelagic sediments, calculated based on consolidation testing results, is less than 4% larger than the function fit to the observations [*Giambalvo et al.*, 2000]. For the fine-grained turbidites, the calculated porosity is less than 10% smaller than the fit to the observations in the upper 10 m of the sediment column and less than 5% smaller throughout the remainder of the sediment column. Differences in sediment permeability due to differences in porosity are less than 30% for the hemipelagic sediment and less than 20% for the fine-grained turbidites. These variations are small relative to the more than two order of magnitude differences in permeability between sediment type, or with depth in a >50 m thick sediment column).

[29] Sediment physical properties vary consistently with the proportion of hemipelagic sediment. Compression index increases with proportion of hemipelagic material, from 0.5 at 30% hemipelagic to 1.4 at 95% hemipelagic (Figure 11a). The systematic increase in compression index with proportion hemipelagic sediment is likely a function of randomly oriented clays within hemipelagic sediment that align under an applied load [*Giambalvo et al.*, 2000]. Permeability at a void ratio of 1 (50% porosity) decreases with proportion of hemipelagic material, from 2×10^{-16} m^2 at 30% hemipelagic sediment to 6×10^{-18} m^2 at 95% hemipelagic sediment (Figure 11b). The systematic decrease in permeability (at a given porosity) with proportion of hemipelagic sediment may indicate that a larger fraction of the pore space within the hemipelagic sediment is not well connected (i.e., lower effective porosity) than in fine-grained turbidites.

7.2. Spatial Variability in Sediment Hydraulic Impedance

[30] Local variations in sediment type and thickness affect the pattern of fluid flow through the sediments. Relatively high fluid upwelling speeds are found at sites with relatively low hydraulic impedance. Therefore fluid seepage is most likely to occur at sites with a combination of thin sediment cover and high sediment permeability. We use the modeled 3-D distribution of sediment types to predict spatial variations in sediment physical properties (consolidation and permeability). At each point in our model of the study area we used the consolidation relationship, which is a function of sediment type, to determine sediment bulk density, effective stress, and porosity at 1 m increments from the seafloor to the basement. We determine the bulk density, effective stress, and porosity by bootstrapping from the seafloor to the basement. For 1 m increments of sediment (beginning at the top of the sediment column), we begin with an assumed sediment bulk density. That bulk density is used to calculate an effective stress. Then the laboratory determined relationship between void ratio and effective stress is used to calculate porosity. With this porosity, the sediment bulk density is recalculated and the procedure is repeated until the change in porosity between iterations is less than 0.05%. With the porosity and

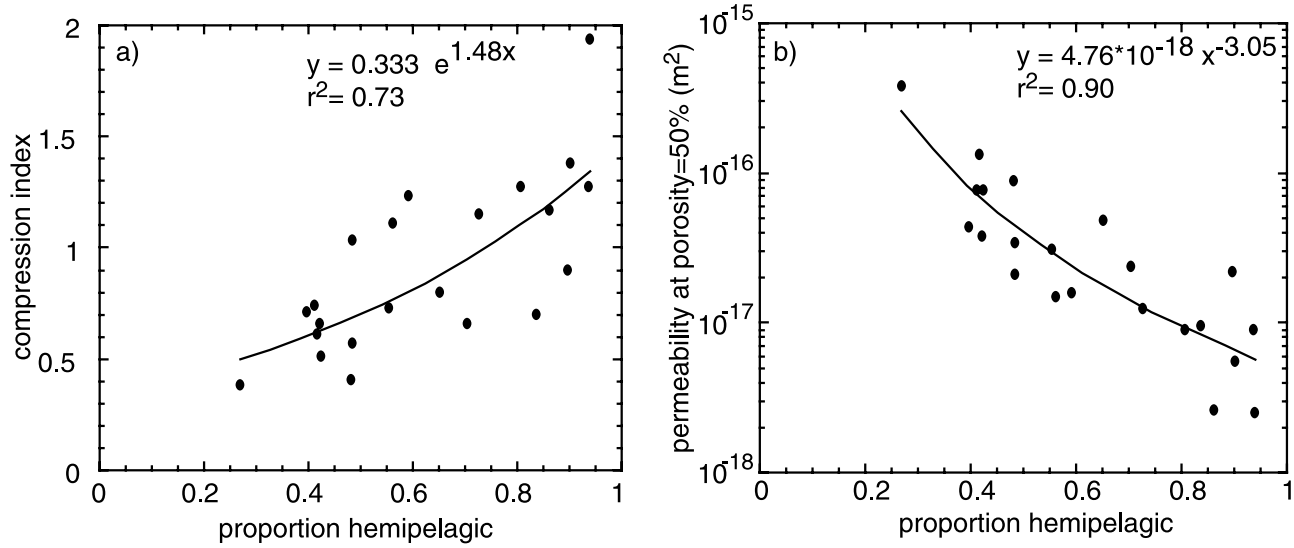

Figure 11. Variations in sediment physical properties with sediment type. (a) The compression index (a measure of the ease of consolidation) increases as the proportion of hemipelagic material within a sample increases. (b) At a given porosity, sediment permeability decreases with increasing proportion hemipelagic material. The relationships between sediment physical properties and sediment type are used with the spatial variations in sediment type (Figures 8 and 9) to model vertical sediment hydraulic impedance throughout the study area.

bulk density of the uppermost 1 m calculated, the procedure is repeated down through the sediment column, the effective stress increasing and porosity decreasing down through the entire sediment column. We use the porosity and sediment type at each depth to determine the permeability of each 1 m section from the seafloor to the basement, and then determine the vertical sediment hydraulic impedance for sediment columns throughout the study area by numerically integrating:

$$I = \int_0^{z'} \frac{dz}{k(z)} \tag{5}$$

where k is permeability. Vertical sediment hydraulic impedance varies from approximately 1×10^{16} m^{-1} to 5×10^{18} m^{-1} overlying the First Ridge, and increases to a maximum value of 1.6×10^{19} m^{-1} off of the ridge, where the sediment column is approximately 300 m thick.

8. Driving Forces

8.1. Basement Overpressure at ODP Sites

[31] The rate of fluid flow through First Ridge sediments and the vertical hydraulic impedance of the sediment have been used previously to estimate the fluid overpressure (pressure above hydrostatic) in basement necessary to drive the flow. Fluid overpressure in First Ridge basement was estimated at <5 kPa [*Giambalvo et al.*, 2000], using a flow rate of 2 mm/yr [*Shipboard Scientific Party*, 1997b] and vertical sediment hydraulic impedance derived from the consolidation and permeability of relatively deep sediment samples [*Giambalvo et al.*, 2000]. Recent modeling of pore water chemistry data at 1030 and 1031 with advection-diffusion-reaction equations yield fluid seepage rates of 1.9 and 3.2 mm/yr, respectively [*Giambalvo et al.*, 2002]. We estimate the fluid overpressure in basement at Site 1031 based on a seepage rate of 3.2 mm/yr and a vertical sediment hydraulic impedance derived from both shallow and deep hemipelagic sediment samples. The sediment column at Site 1031 is predominantly hemipelagic mud with very few, thin, fine-grained turbidite layers [*Shipboard Scientific Party*, 1997b]. We use the average of the consolidation and permeability results for the shallow (<8 m) hemipelagic samples to determine the permeability of sediments from the seafloor to 14 m below seafloor; from 14 m below seafloor to the basement we use the sediment physical properties data for the deep (>20 m) samples [*Giambalvo et al.*, 2000]. Our resulting estimate of fluid overpressure in basement at Site 1031 is 13 kPa. This larger overpressure than previously determined by *Giambalvo et al.* [2000] results from both the increased seepage rate and reduced permeability of the shallow sediments.

8.2. Spatial Variations in Basement Overpressure

[32] We estimate the basement fluid overpressure throughout the study area in order to assess if a reasonable set of driving forces combined with sediment properties information allows the prediction of seepage rates. We have calculated the basement fluid overpressure at Site 1031, but observations from sealed seafloor observatories and results from regional fluid and heat transport models indicate that basement fluid overpressure on the eastern flank of the Juan de Fuca Ridge is spatially variable. Observations from a sealed seafloor observatory [*Davis et al.*, 1992b] at Site 1025 (~5 km west of the First Ridge) suggest basement fluid overpressure on the order of 3 kPa [*Davis and Becker*, 2002]. The overpressure at Site 1025 is ~10 kPa lower than the overpressure calculated at Site 1031; the top of the basement at Site 1025 is ~80 m below the top of basement at Site 1031.

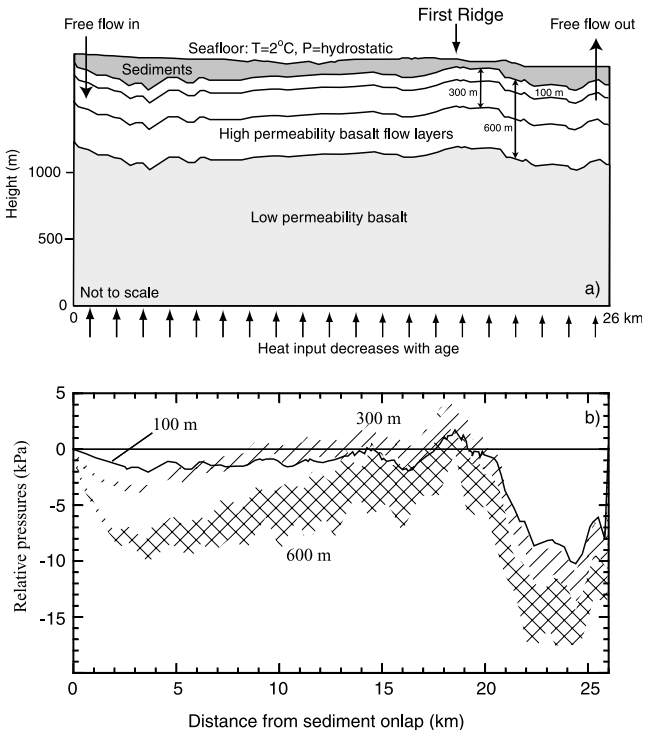

Figure 12. (a) Regional fluid and mass transport model and (b) modeled basement fluid overpressures [modified from *Stein and Fisher*, 2003]. The trend of increasing basement fluid overpressure with increasing elevation of the top of basement is used to estimate overpressures on and around the First Ridge. Modeled pressures in the 300 and 600 m cases are transient on timescales of decades to centuries, therefore the relative pressure at any point in the model covers a range of values.

[33] Numerical modeling of regional scale fluid and heat transport on the eastern flank of the Juan de Fuca Ridge also indicates that basement fluid overpressure may be related to the elevation of the top of basement [*Stein and Fisher*, 2003]. Two-dimensional coupled heat and fluid flow models simulate fluid entering the crust at the point of sediment onlap and moving eastward through a relatively high permeability layer of upper crust capped by relatively low permeability sediments (Figure 12). The basement fluid pressures, permeability, and the lateral flow rate required for modeled seafloor heat flow to match observations all vary with the thickness of the permeable basement layer. However, a similar trend of basement fluid overpressures is calculated over all the permeable basement layer thicknesses tested. Basement fluid overpressure decreases for ~5 km east from the point of sediment onlap, then gradually increases to the First Ridge. Fluid overpressures increase more abruptly, by 3–4 kPa, crossing the First Ridge; overpressures drop significantly to the east of the First Ridge [*Stein and Fisher*, 2003]. The trend of increasing basement fluid overpressure with increasing basement elevation is robust. Similar patterns of high fluid overpressures in basement ridges relative to basement troughs have been suggested elsewhere [*Fisher et al.*, 1990, 1994; *Davis et al.*, 1997; *Wang et al.*, 1997]. However, the details of the modeled pressure distribution on the Juan de Fuca Ridge flank were not used to assess the validity of the heat and mass transport models of *Stein and Fisher* [2003].

[34] Therefore we use the trend of an overpressure versus basement elevation relationship derived from the regional models, but we adjust the overpressure values to closely approximate the observed or calculated overpressure at ODP sites. We average the modeled basement fluid overpressures for the three "free flow" simulations from *Stein and Fisher* [2003] (cases with high-permeability upper basement thickness of 100, 300, and 600 m; Figure 12). Modeled basement fluid overpressures are scaled, with a multiplier, such that the overpressure at Site 1031 is 13 kPa. Basement elevation throughout our study area is used to calculate basement fluid overpressure based on a function fit to the overpressure versus basement elevation data (Figure 13). Along the First Ridge, variations in basement fluid overpressure are small; overpressures range from 10 to 12 kPa. The modeled basement fluid overpressure at Site 1031 is 12 kPa; at Site 1025 the modeled overpressure is 6 kPa. The modeled overpressures approximate the observations and are consistent with the trend of increasing overpressure with basement elevation suggested by *Stein and Fisher* [2003].

[35] In modeling the fluid seepage rate through the sediments based on basement fluid overpressure and sediment hydraulic impedance, we perform separate calculations for two cases: 1) with the modeled spatial variations in overpressure described above, and 2) with constant overpressure. As the spatial variations in basement overpressure away from Sites 1031 and 1025 are not well constrained, the

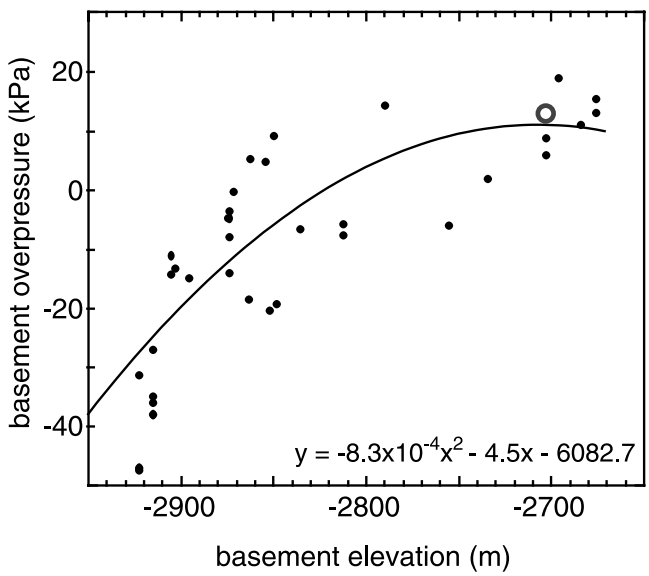

Figure 13. Variations in basement fluid overpressure with basement elevation. At Site 1031 the fluid overpressure in basement is 13 kPa, based on the seepage rate and vertical hydraulic impedance of the sediment column (open circle). Basement fluid overpressures relative to the overpressure at Site 1031 have been modeled along a transect across the First Ridge (solid circles) [*Stein and Fisher*, 2003]. A fit to modeled basement overpressures on and around the First Ridge versus the elevation of the top of basement is used to predict basement fluid overpressure throughout the study area.

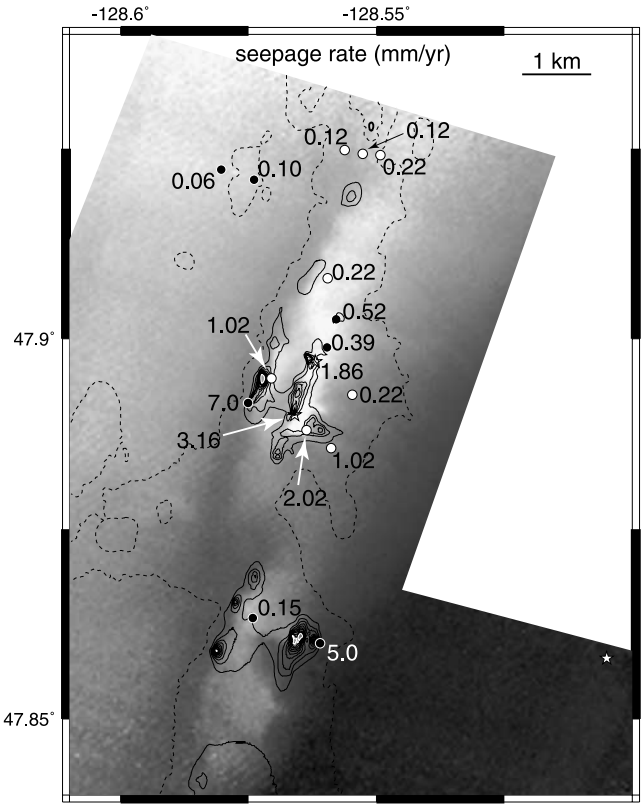

Figure 14. Modeled seepage distribution on the First Ridge. Contours show the modeled fluid seepage distribution overlain on gray scale bathymetry (as shown in Figure 2). The dashed line is the 0 mm/yr contour. The solid lines are 1 mm/yr contours from 1 to 10 mm/yr. Seepage rates in excess of 10 mm/yr, up to 27 mm/yr, occur in isolated areas; 10 and 20 mm/yr contours are shown in white. Point measurements of seepage rates have been determined at ODP sites (star) [*Giambalvo et al.*, 2002], and shallow sediment cores (open circles, *Wheat and Mottl* [1994]; and solid circles, this study).

calculations made with constant overpressure allow us to focus on the spatial variations in fluid seepage rate due to variations in sediment hydraulic impedance alone.

9. Seepage Distribution

[36] We use the continuous estimates of basement fluid overpressure and vertical sediment hydraulic impedance to generate a map of predicted fluid seepage rates on and around the First Ridge (Figure 14). In the following discussions the "modeled" or "calculated" seepage rates refer to fluid seepage rates determined from the basement fluid overpressure and sediment hydraulic impedance; "measured" or "observed" seepage rates refer to those determined from pore water chemistry profiles. The modeled seepage rates range from 0 to 27 mm/yr. Most of the large amplitude spatial fluctuations in seepage rates occur over the First Ridge. The average modeled seepage rate over the entire 11 km length of the First Ridge within our study area is 1.3 mm/yr, slightly less than the average of the 15 point measurements of seepage rates overlying the ridge determined from pore water chemistry profiles, 1.5 mm/yr. On the basis of the model results, half of the total volume flux of seepage to the study area is contributed from the 2% of the study area with flow rates >1.6 mm/yr. Only considering the area overlying the First Ridge, half of the volume flux is contributed from 25% of the area, with flow rates ≥1.1 mm/yr. The lowest fluxes from the First Ridge occur at the northern end of the study area and in the offset in the axis of the First Ridge, south of Site 1031. The highest fluxes occur in two sections of the ridge, one that includes Site 1031 and one immediately south of the offset in the axis of the First Ridge. Along both of these sections of the First Ridge maximum calculated seepage rates are in excess of 10 mm/yr. The model slightly overpredicts very slow flow rates and underpredicts high seepage rates derived from the pore water chemistry (Figure 15).

[37] Of the primary controls on fluid seepage rate, sediment thickness on and around the First Ridge is the best constrained; basement overpressure and sediment type are less well constrained. Seepage rate varies directly with basement overpressure (given constant hydraulic impedance). We calculate the fluid seepage rate with a constant

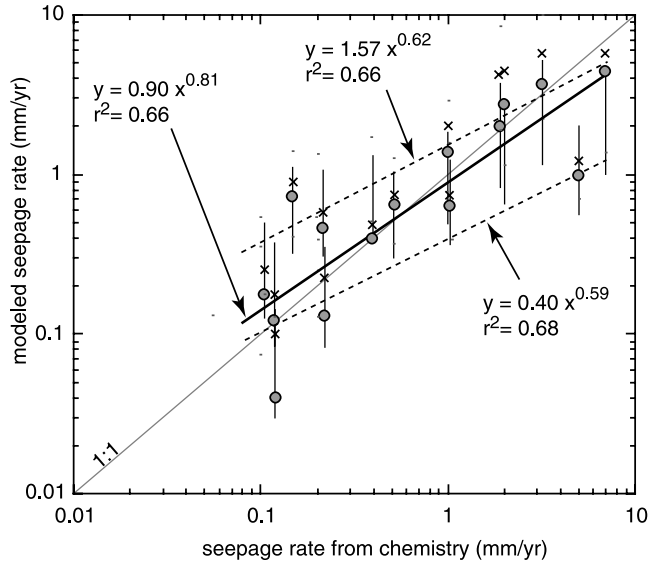

Figure 15. Modeled versus observed seepage rates. Observed seepage rates are determined by fitting solutions of an advection-diffusion equation to sediment core pore water chemistry profiles [*Wheat and Mottl*, 1994; *Giambalvo et al.*, 2002; this study]. Modeled seepage rates (circles) are derived from the spatial distribution of basement fluid overpressure and sediment physical properties. The vertical lines show the range of possible seepage rates as a result of variations in sediment type (i.e., sediment physical properties). Most of the observed variation in seepage rate can be explained by variations in sediment properties; crosses indicate modeled seepage rates calculated with constant basement fluid overpressure of 13 kPa. The solid gray line is the ideal, linear correlation between modeled and observed data. The best fit to the data is shown with a solid line. Dashed black lines show regressions to the maximum and minimum possible seepage rates with the modeled basement fluid overpressures (ends of vertical lines) versus observed seepage rates.

basement fluid overpressure (13 kPa, i.e., the calculated overpressure at Site 1031), to demonstrate the dominance of variations in sediment hydraulic impedance in controlling the fluid seepage pattern. While the fit between the modeled and observed seepage rates is best when using the modeled basement fluid overpressure (circles on Figure 15), the calculated seepage rates with constant overpressure (crosses on Figure 15) show large variations in seepage rate due only to variations in hydraulic impedance of the same scale as the observations. At a given location, variations in sediment type can result in variations in seepage rate of almost an order of magnitude (see vertical bars in Figure 15).

10. Comparison Between Seepage Distribution and Seismic Anomalies

[38] Narrow zones of reduced seismic reflection amplitudes have been described within the sediments on and around the First Ridge [*Zühlsdorff et al.*, 1999; *Zühlsdorff and Spieß*, 2001]. Reflection anomalies are observed at all seismic source frequencies, but are most prominent in the Parasound data (i.e., at high source frequency range) (Figure 16) [*Zühlsdorff et al.*, 1999]. The low-reflection amplitude anomalies generally occur over buried basement highs and have previously been mapped (Figure 17). These low seismic reflection amplitude anomalies are inferred to result from elevated sediment porosity, which causes a decrease in reflection coefficient and an increase in seismic attenuation [*Zühlsdorff et al.*, 1999]. In order to explain the largest magnitude seismic reflectivity anomalies with porosity variations, sediment porosity within the seismic anomalies must be on the order of 15–20% higher than porosity outside of the anomalies [*Zühlsdorff et al.*, 1999].

[39] The distributions of seismic reflectivity anomalies and modeled fluid seepage were derived using separate methods that function on different scales so a comparison should be done cautiously; but differences in sediment physical properties contribute to both phenomena, therefore an examination of the two sets of observations is instructive. Zones of reduced seismic reflectivity in the northern part of the study area generally correspond to areas with high modeled fluid seepage rates (Figure 16). Low-reflectivity anomalies that are continuous up to the seafloor primarily occur in areas with modeled seepage rates >0.25 mm/yr; many occur in locations with seepage rates >1 mm/yr.

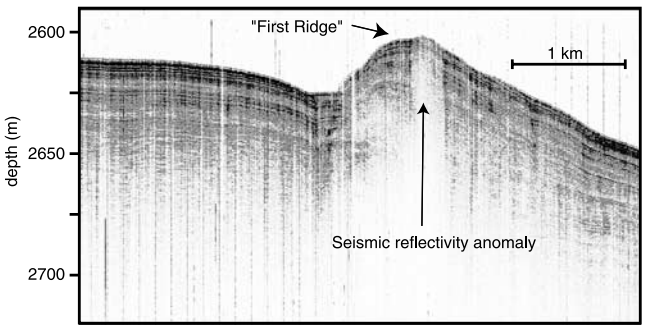

Figure 16. Line of Parasound data across the First Ridge. Seismic reflectivity is anomalously low overlying the First Ridge. The seismic anomalies have been inferred to result from elevated porosities [*Zühlsdorff et al.*, 1999].

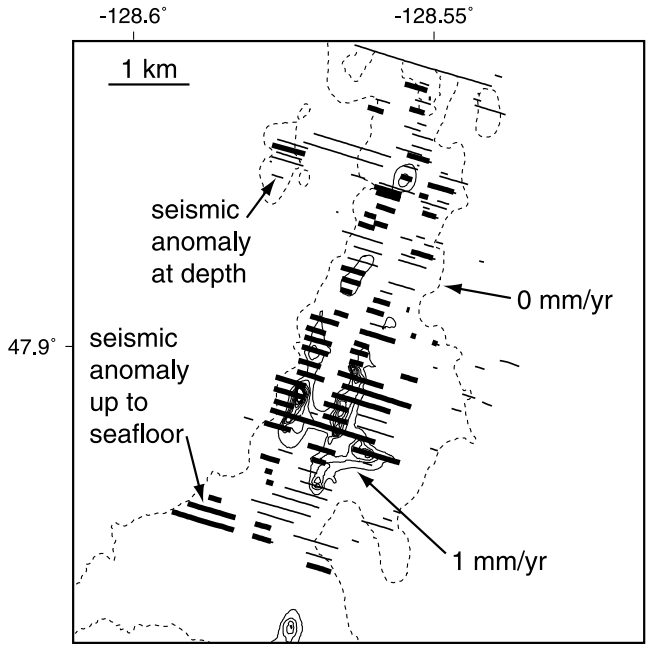

Figure 17. Relation between modeled fluid seepage rate and reflection seismic amplitude anomalies. Seismic anomalies generally occur in areas with high seepage rates. Seismic anomalies result from variations in sediment physical properties; fluid seepage patterns are influenced by variations in the same properties.

However, some of these seismic anomalies occur in areas with low seepage rates (<0.25 mm/yr), and some areas of rapid seepage (>1 mm/yr) are areas of normal seismic reflection amplitude. Low-reflectivity anomalies at depth in the sediment column occur both in zones of high and low modeled seepage rate. In principle there are several mechanisms which could explain the areas of locally elevated porosity that could cause the observed seismic anomalies. These include: 1) dissolution of sediment grains during diagenesis, 2) locally elevated fluid pressure (maintaining a low effective stress and inhibiting sediment consolidation), and 3) spatial variability in sediment type.

[40] Significantly enhanced sediment porosity resulting from the dissolution of sediment grains during diagenesis is unlikely in this setting. Fine-grained sediments from Sites 1030 and 1031, where fluid seepage rates are 1.9 and 3.2 mm/yr, respectively, have been examined with a scanning electron microscope. The samples contained partially dissolved foraminifera and nannofossils, but no significant secondary porosity was observed [*Giambalvo et al.*, 2000].

[41] Spatial variations in both fluid pressure and sediment type can result in lateral variations in sediment porosity. Sediment physical property data indicate that sediment porosity on and around the First Ridge varies with sediment type, with hemipelagic sediments having higher porosity than fine-grained turbidites. Sediment of a given type can have a range of porosity versus depth profiles depending on the local fluid pressure or diagenetic history. Fluid overpressure that is maintained in sediments throughout sediment deposition will maintain a lower effective stress in the sediment; sediment will consolidate less and have

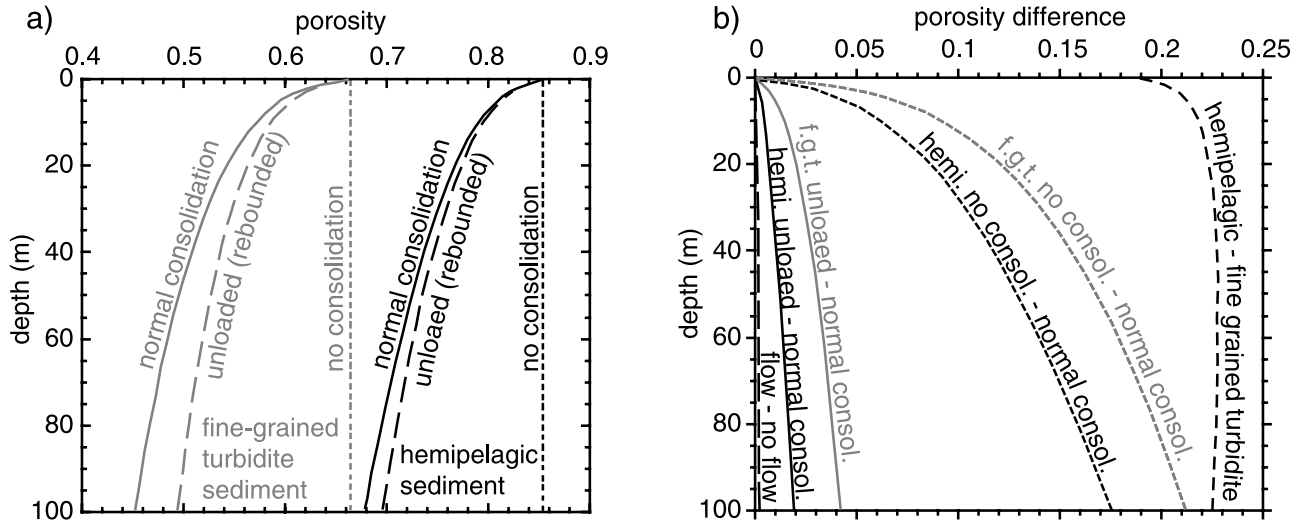

Figure 18. Porosity versus depth for fine-grained turbidite (gray) and hemipelagic (black) sediment columns. For each extreme sediment type, potential porosities fall between the normal consolidation (solid) and no consolidation (small dashed) profiles (Figure 18a). No consolidation requires fluid pressures maintained at lithostatic or a mechanical means of preventing consolidation. The highest porosities that can be achieved by increasing fluid pressures in sediment that has been consolidated are indicated on the unloaded (long dashed) profiles. Overpressures within the range of those observed in basement around the First Ridge have a minimal impact on porosities of both sediment type (flow/no flow profile; Figure 18b). Transient fluid overpressures up to lithostatic values can increase porosities by <5% (unloaded/normal consolidation profiles; Figure 18b). Adjacent columns of fine-grained turbidite and hemipelagic sediment will have ~20% differences in porosity (hemipelagic–fine-grained turbidite profile; Figure 18b).

increased porosity relative to sediment with hydrostatic fluid pressures (i.e., no overpressure). In the most extreme case, if fluid overpressures remain at lithostatic throughout sediment deposition, the sediments do not consolidate. Fluid overpressure can also reduce the effective stress of sediment that has already been consolidated. Such an increase in porosity is due to the elastic rebound of sediment grains and its magnitude is somewhat limited. On the basis of our consolidation experiments, the porosity of a fine-grained turbidite sediment column that is normally consolidated with hydrostatic fluid pressures will decrease from ~66% at the seafloor to ~45% 100 m below seafloor (mbsf) (Figure 18a). In order to maintain lithostatic pressures (and not consolidate the sediment) throughout a fine-grained turbidite sediment column 100 m thick, the fluid overpressure in basement would have to be ~800 kPa. The normal consolidation and no consolidation porosity profiles delineate the range of possible porosities within fine-grained turbidite sediment columns (Figure 18a). The porosities of fine-grained turbidites deposited with fluid overpressures maintained at the estimated values over the First Ridge (~13 kPa at the sediment-basement contact) are <0.2% higher than in sediment with no fluid overpressure. The highest porosities that can be achieved in a 100 m thick sediment column of rebounded fine-grained turbidites (normally consolidated fine-grained turbidites which are then subjected to lithostatic fluid pressures) are ~4% higher than in normally consolidated sediments (see "unloaded" porosity profile in Figure 18a). If overpressures (and fluid seepage) are transient, sediment porosity will vary between the "normal consolidation" and "unloaded" porosity profiles (Figure 18a), barring any mechanical process inhibiting consolidation. Hemipelagic sediments have higher porosities than fine-grained turbidites, but show similar trends in porosity given the same consolidation histories (Figure 18a). In all cases, differences in porosity between two columns of the same type of sediment with different fluid overpressure histories are largest at depth and decrease to zero at the seafloor, where there is no overburden (Figure 18b). Deep hemipelagic sediment samples at sties 1030 and 1031 are slightly overconsolidated [*Giambalvo et al.*, 2000], also suggesting that large fluid pressures have not increased sediment porosity. Preconsolidation stresses could not be determined for the shallow sediment samples tested (i.e., they began consolidating on the virgin consolidation curve).

[42] The difference in porosity between normally consolidated fine-grained turbidite and hemipelagic sediment columns shows less variation with depth and ranges from ~18–23% (Figure 18b). However, we have not explicitly identified a process which could generate significant variations in sediment type over short distances (e.g., Figure 16) in this setting. While turbidite deposition around topography can result in lateral variations in sediment type, we have only very general estimates for the hydrodynamic properties of turbidity currents at these sites and therefore do not have precise estimates of the distance over which dramatic facies changes could occur over the First Ridge. Additionally, our simple model of sediment type distribution does not mimic the pattern of seismic anomalies in all locations. Fine-grained sediments from shallow piston cores on the First Ridge north of Site 1030 have a high proportion of fine-grained turbidites (and relatively low porosity). In our

simple sediment distribution model, the near surface sediments in this area are primarily fine-grained turbidites and they increase in proportion hemipelagic with depth. This is not consistent with elevated porosities (relative to sediments off the First Ridge) in shallow sediments in the area, predicted based on the presence of seismic anomalies. For all the shallow fine-grained sediments associated with seismic anomalies north of Site 1030 to have elevated porosities, either the sediments are more hemipelagic than represented in our simple model, or additional, unknown processes have acted to maintain elevated porosities in the narrow zones of the reflectivity anomalies. If the shallow sediments north of Site 1030 were modeled as primarily hemipelagic, the permeability of the sediments would be greater. As a result either the modeled seepage rates in this area would increase and the agreement between modeled and observed seepage rates would be reduced (Figure 15), or the basement overpressures would need to be only ~4–8 kPa (instead of the 13 kPa, as modeled) in order to maintain the relatively low seepage rates though higher permeability sediments. Spatial variations in basement overpressure are not well constrained; basement overpressure could vary laterally as a result of convection geometry and permeability distribution in basement.

11. Summary and Conclusions

[43] A mix of hemipelagic and turbidite sediment has accumulated on and around the First Ridge. Sandy turbidite deposition is limited to sites off of the First Ridge and overlying the ridge where the seafloor is relatively flat (i.e., basement ridge topography has been largely obscured by overlying sediment accumulation and is not expressed on the seafloor). Some silty turbidites are found at sites overlying basement that is draped with a thin blanket of sediment, where muted basement topography is expressed on the seafloor. Where the topographic ridge is more prominent, hemipelagic sediment accumulation dominates. This is consistent with turbidites sourced on the continental margin being blocked or diverted by the topographic high (i.e., portions of the First Ridge). Seismic stratigraphy [*Zühlsdorff and Spieß*, 2001] and the timing of turbidite deposition (Underwood et al., submitted manuscript, 2002) suggest that the First Ridge separates different sedimentation regimes to the east and west, and large events affecting both sides of the ridge simultaneously are rare [*Zühlsdorff and Spieß*, 2001]. As a result, a mix of hemipelagic and turbiditic sediments have accumulated at sites off the topographic ridge, while primarily hemipelagic sediments have accumulated on the topographic ridge.

[44] Topography on the order of 50 m appears to influence the distribution of turbidite sediment in this area. Assuming reasonable turbidity current properties (4% suspended sediment concentration, and velocities ranging from 1 to 10 m/s), this would suggest that many of the turbidity currents that entered this area were <25–40 m thick. As the basins surrounding the First Ridge are progressively filled, reducing ridge relief, turbidite emplacement may advance along the ridge to the south.

[45] Sediment thickness and type strongly influence seepage rates on and around the sediment-covered First Ridge on the eastern flank Juan de Fuca Ridge. In this region, seepage has been detected at sites with relatively thin blankets of high-porosity (and relatively high permeability) hemipelagic sediments. In other areas, the thicker sediment cover associated with fine-grained turbidites acts to isolate the basement hydraulically and divert seepage elsewhere.

[46] Knowledge of spatial variations in sediment hydraulic properties is necessary to predict fluid seepage patterns accurately. Spatially continuous estimates of fluid seepage rate are determined from the distribution of basement fluid overpressure, sediment thickness, and sediment type. Variations in sediment thickness and basement fluid overpressure in this area result in seepage rate variations of approximately 2 orders of magnitude. Variations in sediment type can alter seepage rates by an order of magnitude. Modeled fluid seepage rates range from 0 to 27 mm/yr and capture much of the spatial variability in observed seepage rates from pore water chemistry profiles. A comparison of the observed seepage pattern and sediment distribution on the First Ridge suggests that sediment thickness and type can explain much of the seepage pattern, without requiring focused flow along faults or zones of anomalous sediment permeability.

[47] More than 90% of the total volume flux of fluid from sediments in the study area is discharged through sediments overlying the First Ridge. On most of the First Ridge, seepage rates are in excess of 0.25 mm/yr. Focused seepage dominates the volume flux from the First Ridge; half of the volume flux is contributed from 25% of the area, with flow rates $\geq$1.1 mm/yr. Although there are relatively steep lateral gradients in seepage rate, on the order of 10 mm/yr over 200 m, vertical chemical gradients in shallow pore water are still ~200 times larger than lateral gradients.

[48] The spatial distribution of both fluid seepage and seismic reflectivity anomalies are influenced by variations in sediment physical properties. Most areas with relatively high fluid seepage rates correspond to areas of seismic reflectivity anomalies which have been shown to be areas of elevated porosity; some areas of high seepage rate do not contain seismic anomalies and some seismic anomalies occur in locations with little or no seepage. Zones of elevated porosities could result from lateral variations in fluid pressure and sediment type. Fluid pressures maintained at lithostatic throughout sediment deposition could result in porosity anomalies in the range of 17–21%, 100 mbsf, but require basement fluid overpressures more than 30 times larger than observed at Site 1025 [*Davis and Becker*, 2002] or calculated for Site 1031. Spatially variable fluid pressures within a constant sediment type can not increase the porosity of shallow sediments sufficiently to explain the seismic anomalies (even with extraordinarily large basement overpressures). Local zones of high porosity may be areas with relatively high seepage rates, but the high porosities are not caused by fluid overpressures.

[49] Spatial variations in sediment type could result in porosity anomalies on the order of 20% throughout the sediment column, within the range predicted by analysis of seismic anomalies. However, we can not explicitly document the processes in this area that would result in large variations in sediment type over relatively short distances. It is unclear how porosity differences on the order of 20% over relatively short distances on and around the First Ridge are created or maintained. The results of this study can not

rule out either spatial variations in sediment type due to the interactions of turbidity currents with seafloor topography, or some as yet unknown nondepositional process acting in narrow zones as suggested by [*Zühlsdorff et al.*, 1999]. Since the narrow zones of decreased reflection amplitudes indicate smaller scale features, and since areas with high seepage rates do not exactly match those seismic anomalies, the seismic anomalies appear to be not completely covered by our conceptual model of sediment type distribution and may have to be considered again separately.

[50] Basement topography affects basement fluid overpressures and influences sediment depositional processes. The combination of enhanced overpressures and complex depositional patterns can explain much of the unique pattern in fluid seepage around a buried basement ridge on the Juan de Fuca Ridge flank. Variations in sediment physical properties contribute to both variations in fluid seepage rate and seismic reflectivity. Coordinated transects of long sediment cores and reflection seismic data across both zone of fluid seepage and seismic reflectivity anomalies are required in order to complete a detailed comparison of sediment physical properties and the seismic response of sediments in these settings.

[51] **Acknowledgments.** Support for this project has been provided by NSF grant OCE-9819242 to Andrew Fisher. We thank Liz Screaton and Keir Becker for helpful suggestions that improved the manuscript. Maps were created using GMT [*Wessel and Smith*, 1998].

References

Alexander, J., and S. Morris (1994), Observations on experimental, nonchannelized, high-concentration turbidity currents and variations in deposits around obstacles, *J. Sediment. Res., Sect. A*, *64*(4), 899–909.

Alt, J. C., and D. A. H. Teagle (1999), The uptake of carbon during alteration of ocean crust, *Geochim. Cosmochim. Acta*, *63*(10), 1527–1535.

Alt, J. C., J. Honnorez, C. Laverne, and R. Emmermann (1986), Hydrothemal alteration of a 1-km section through the upper oceanic crust, Deep Sea Drilling Project Hole 504B: Mineralogy, chemistry, and evolution of seawater-basalt interaction, *J. Geophys. Res.*, *91*, 10,309–10,335.

Anderson, R. N., and M. A. Hobart (1976), The relation between heat flow, sediment thickness, and age in the eastern Pacific, *J. Geophys. Res.*, *81*, 2968–2989.

Baines, P. G. (1979), Observations of stratified flow past three-dimensional barriers, *J. Geophys. Res.*, *84*, 7834–7838.

Berner, R. A. (1980), *Early Diagenesis: A Theoretical Approach*, 241 pp., Princeton Univ. Press, Princeton, N. J.

Davis, E. E., and K. Becker (2002), Observations of natural-state fluid pressures and temperatures in young oceanic crust and inferences regarding hydrothermal circulation, *Earth Planet. Sci. Lett.*, *204*, 231–248.

Davis, E. E., et al. (1992a), An experiment to study the nature of hydrothermal circulation n young oceanic crust, *Can. J. Earth Sci.*, *29*, 925–952.

Davis, E. E., K. Becker, T. Pettigrew, B. Carson, and R. MacDonald (1992b), CORK: A hydrogeologic seal and downhole observatory for deep-ocean boreholes, *Proc. Ocean Drill. Program Initial Rep.*, *139*, 43–53.

Davis, E. E., K. Wang, J. He, D. Chapman, H. Villinger, and A. Rosenberger (1997), An unequivocal case for high Nusselt number hydrothermal convection in sediment-buried igneous oceanic crust, *Earth Planet. Sci. Lett.*, *146*, 137–150.

Elderfield, H., and A. Schultz (1996), Mid-ocean ridge hydrothermal fluxes and the chemical composition of the ocean, *Annu. Rev. Earth Planet. Sci.*, *24*, 191–224.

Fisher, A., K. Becker, T. N. Narasimhan, M. Langseth, and M. Mottl (1990), Passive, off-axis convection on the southern flank of the Costa Rica Rift, *J. Geophys. Res.*, *95*, 8845–8858.

Fisher, A. T., K. Becker, and T. N. Narasimhan (1994), Off-axis hydrothermal circulation: Parameteric tests of a refined model of precesses at Deep Sea Drilling Project/Ocean Drilling Program Site 504, *J. Geophys. Res.*, *99*, 3097–3121.

Giambalvo, E. R., A. T. Fisher, J. T. Martin, L. Darty, and R. P. Lowell (2000), Origin of elevated sediment permeability in a hydrothermal seepage zone, eastern flank of the Juan de Fuca Ridge, and implications for transport of fluid and heat, *J. Geophys. Res.*, *105*, 913–928.

Giambalvo, E. R., C. I. Steefel, A. T. Fisher, N. D. Rosenberg, and C. G. Wheat (2002), Effect of fluid-sediment reaction on hydrothermal fluxes of major elements, eastern flank of the Juan de Fuca Ridge, *Geochim. Cosmochim. Acta*, *66*(10), 1739–1757.

Ginster, U., M. J. Mottl, and R. P. Von Herzen (1994), Heat-flux from black smokers on the Endeavor and Cleft segments, Juan de Fuca Ridge, *J. Geophys. Res.*, *99*, 4937–4950.

Haughton, P. D. W. (1994), Deposits of deflected and ponded turbidity currents, Sorbas Basin, southeast Spain, *J. Sediment. Res., Sect. A*, *64*(2), 233–246.

Imbrie, J., J. D. Hays, D. G. Martinson, A. McIntyre, A. C. Mix, J. J. Morley, N. G. Pisias, W. L. Prell, and N. J. Shackleton (1984), The orbital theory of Pleistocene climate: Support from a revised chronology of the marine $\delta^{18}O$ record, in *Milankovitch and Climate, Part 1, NATO ASI series. Ser. C*, *Math. Phys. Sci.*, vol. 126, edited by A. L. Berger et al., pp. 269–305, Kluwer Acad., Norwell, Mass.

Jacobson, R. S. (1992), Impact of crustal evolution on changes of the seismic properties of the uppermost ocean crust, *Rev. Geophys.*, *30*(1), 23–42.

Johnson, H. P., K. Becker, and R. P. Von Herzen (1993), Near-axis heat flow measurements on the northern Juan de Fuca Ridge: Implications for fluid circulation in oceanic crust, *Geophys. Res. Lett.*, *20*(17), 1875–1878.

Kappel, E. S., and W. B. F. Ryan (1986), Volcanic episodicity and a non-steady state rift valley along Northeast Pacific spreading centers: Evidence from Sea MARC I, *J. Geophys. Res.*, *91*, 13,925–13,940.

Karato, S., and K. Becker (1983), Porosity and hydraulic properties of sediments from the Galapagos spreading center and their relationship to hydrothermal circulation in the oceanic crust, *J. Geophys. Res.*, *88*, 1009–1017.

Kneller, B., and C. Buckee (2000), The structure and fluid mechanics of turbidity currents: A review of some recent studies and their geological implications, *Sedimentology*, *47*, *Suppl. 1*, 62–94.

Kneller, B., and W. McCaffrey (1999), Depositional effects of flow nonuniformity and stratification within turbidity currents approaching a bounding slope: Deflection, reflection, and facies variation, *J. Sediment. Res.*, *69*(5), 980–991.

Kneller, B., D. Edwards, W. McCaffrey, and R. Moore (1991), Oblique reflection of turbidity currents, *Geology*, *14*, 250–252.

Langseth, M. G., M. J. Mottl, M. A. Hobart, and A. T. Fisher (1988), The distribution of geothermal and geochemical gradients near Site 501/504, implications for hydrothermal circulation in the oceanic crust, *Proc. Ocean Drill. Program Initial Rep.*, *111*, 23–32.

Li, Y.-H., and S. Gregory (1974), Diffusion of ions in sea water and in deep-sea sediments, *Geochim. Cosmochim. Acta*, *38*, 703–714.

Lister, C. R. B. (1972), On the thermal balance of a mid-ocean ridge, *Geophys. J. R. Astron. Soc.*, *26*, 515–525.

Maris, C. R. P., and M. L. Bender (1982), Upwelling of hydrothermal solutions through ridge flank sediments shown by pore water profiles, *Science*, *216*(7), 623–626.

Maris, C. R. P., M. L. Bender, P. N. Frolich, R. Barnes, and N. A. Luedtke (1984), Chemical evidence for advection of hydrothermal solutions in the sediments of the Galapagoes Mounds Hydrothermal Field, *Geochim. Cosmochim. Acta*, *48*, 2331–2346.

McDuff, R. E. (1981), Major cation gradients in DSDP interstitial waters: The role of diffusive exchange between seawater and upper oceanic crust, *Geochim. Cosmochim. Acta*, *45*, 1705–1713.

Middleton, G. V. (1993), Sediment deposition from turbidity currents, *Annu. Rev. Earth Planet. Sci.*, *21*, 89–114.

Mottl, M. J. (1989), Hydrothermal convection, reaction and diffusion in sediments on the Costa Rica Rift flank, pore water evidence from ODP Sites 677 and 678, *Proc. Ocean Drill. Program Sci. Results*, *111*, 195–214.

Mottl, M. J., and C. G. Wheat (1994), Hydrothermal circulation through mid-ocean ridge flanks: Fluxes of heat and magnesium, *Geochim. Cosmochim. Acta*, *58*, 2225–2237.

Mottl, M. J., C. G. Wheat, E. Baker, N. Becker, E. Davis, R. Feely, A. Grehan, D. Kadko, M. Lilley, G. Massoth, C. Moyer, and F. Sansone (1998), Warm springs discovered on 3.5 Ma oceanic crust, eastern flank of the Juan de Fuca Ridge, *Geology*, *26*, 51–54.

Normark, W. R., and D. J. W. Piper (1991), Initiation processes and flow evolution of turbidity currents: Implications for the depositional records, in *From Shoreline to Abyss: Contributions to Marine Geology in Honor of Francis Parker Shepard*, edited by R. H. Osborne, *SEPM Spec. Publ.*, *46*, 207–229.

Olsen, H. W., R. W. Nichols, and T. L. Rice (1985), Low gradient permeability measurements in a triaxial system, *Geotechnique*, *35*(2), 145–157.

Pickering, K. T., and R. N. Hiscott (1985), Contained (reflected) turbidity currents from the Middle Ordovician Cloridorme Formation, Quebec Canada: An alternative to the antidune hypothesis, *Sedimentology*, *32*, 373–394.

Pickering, K. T., M. B. Underwood, and A. Taira (1992), Open-ocean to trench turbidity-current flow in the Nankai Trough: Flow collapse and reflection, *Geology*, *20*, 1099–1102.

Prins, M. A., and G. J. Weltje (1999), End-member modeling of siliclastic grain-size distributions: The Late Quaternary record of eolian and fluvial sediment supply to the Arabian Sea and its paleoclimatic significance, in *Numerical Experiments in Stratigraphy: Recent Advances in Stratigraphic and Sedimentologic Computer Simulations*, edited by J. W. Harbaugh et al., *SEPM Spec. Publ.*, 91–111.

Rottman, J. W., J. E. Simpson, and J. C. R. Hunt (1985), Unsteady gravity current flows over obstacles: Some observations and analysis related to the phase II trials, *J. Hazardous Mater.*, *11*, 325–340.

Rowe, P. W., and L. Barden (1966), A new consolidation cell, *Geotechnique*, *16*, 162–170.

Sclater, J. G., J. Crowe, and R. N. Anderson (1976), On the reliability of oceanic heat flow averages, *J. Geophys. Res.*, *81*, 2997–3006.

Sclater, J. G., C. Jaupart, and D. Galson (1980), The heat flow through oceanic and continental crust and the heat loss of the Earth, *Rev. Geophys.*, *18*(1), 269–311.

Shipboard Scientific Party (1997a), Introduction and summary: Hydrothermal circulation in the oceanic crust and its consequences on the eastern flank of the Juan de Fuca Ridge, *Proc. Ocean Drill. Program Initial Rep.*, *168*, 1–15.

Shipboard Scientific Party (1997b), Buried basement transect (Sites 1028, 1029, 1030, 1031, and 1032), *Proc. Ocean Drill. Program Initial Rep.*, *168*, 161–212.

Shipboard Scientific Party (1997c), Hydrothermal transition transect (Sites 1023, 1024, and 1025), *Proc. Ocean Drill. Program Initial Rep.*, *168*, 49–100.

Snelgrove, S. H., and C. B. Forster (1996), Impact of seafloor sediment permeability and thickness on off-axis hydrothermal circulation: Juan de Fuca Ridge eastern flank, *J. Geophys. Res.*, *101*, 2915–2925.

Snyder, W. H., R. S. Thompson, R. E. Eskridge, R. E. Lawson, I. P. Castro, J. T. Lee, J. C. Hunt, and Y. Ogawa (1985), The structure of strongly stratified flow over hills: Dividing-streamline concept, *J. Fluid Mech.*, *152*, 249–288.

Spinelli, G. A., E. R. Giambalvo, and A. T. Fisher (2004), Sediment permeability, distribution, and influence on fluxes in oceanic basement, in *Hydrogeology of the Oceanic Lithosphere*, edited by E. E. Davis and H. Elderfield, Cambridge Univ. Press, in press.

Stein, C. A., and S. Stein (1994), Comparison of plate and asthenospheric flow models for the thermal evolution of oceanic lithosphere, *Geophys. Res. Lett.*, *21*(8), 709–712.

Stein, J., and A. T. Fisher (2003), Observations and models of lateral hydrothermal circulation on a young ridge flank: Numerical evaluation of thermal and chemical constraints, *Geochem. Geophys. Geosyst.*, *4*(1), doi:10.1029/2002GC000415.

Stow, D. A. V. (1994), Deep sea processes of sediment transport and deposition, in *Sediment Transport and Depositional Processes*, edited by K. Pye, pp. 257–291, Blackwell, Malden, Mass.

Ullman, W. J., and R. C. Aller (1982), Diffusion coefficients in nearshore sediments, *Limnol. Oceanogr.*, *27*(3), 552–556.

Underwood, M. B., and K. D. Hoke (2000), Composition and provenance of turbidite sand and hemipelagic mud in northwestern Cascadia Basin, *Proc. Ocean Drill. Program Sci. Results*, *168*, 51–65.

Wang, K., J. He, and E. E. Davis (1997), Influence of basement topography on hydrothermal circulation in sediment-buried igneous oceanic crust, *Earth Planet. Sci. Lett.*, *146*, 151–164.

Weltje, G. J. (1997), End-member modeling of compositional data: Numerical-statistical algorithms for solving the explicit mixing problem, *Math. Geol.*, *29*(4), 503–549.

Wessel, P., and W. Smith (1998), New, improved version of Generic Mapping Tools released, *Eos Trans. AGU*, *79*, 579.

Wheat, C. G., and R. E. McDuff (1995), Mapping the fluid flow of the Mariana Mounds ridge flank hydrothermal system: Pore water chemical tracers, *J. Geophys. Res.*, *100*, 8115–8131.

Wheat, C. G., and M. J. Mottl (1994), Hydrothermal circulation, Juan de Fuca Ridge eastern flank: Factors controlling basement water composition, *J. Geophys. Res.*, *99*, 3067–3080.

Wheat, C. G., and M. J. Mottl (2000), Composition of pore and spring waters from Baby Bare: Global implications of geochemical fluxes from a ridge flank hydrothermal system, *Geochim. Cosmochim. Acta*, *64*, 629–642.

Williams, D. L., K. Green, T. H. van Andel, R. P. Von Herzen, J. R. Dymond, and K. Crane (1979), The hydrothermal mounds of the Galapagos Rift: Observations with DSRV Alvin and detailed heat flow studies, *J. Geophys. Res.*, *84*, 7467–7484.

Zühlsdorff, L., and V. Spieß (2001), Modeling seismic reflection patterns from Ocean Drilling Program Leg 168 core density logs: Insight into lateral variations in physical properties and sediment input at the eastern flank of the Juan de Fuca Ridge, *J. Geophys. Res.*, *106*, 16,119–16,133.

Zühlsdorff, L., V. Spieß, C. Huebscher, and M. Breitzke (1999), Seismic reflectivity anomalies in sediments at the eastern flank of the Juan de Fuca Ridge: Evidence for fluid migration?, *J. Geophys. Res.*, *104*, 15,351–15,364.

A. T. Fisher, Earth Sciences Department, University of California, Santa Cruz, 1156 High Street, Santa Cruz, CA 95064, USA. (afisher@es.ucsc.edu)

E. R. Giambalvo, Sandia National Laboratories, Carlsbad, NM 88220, USA. (ergiamb@sandia.gov)

M. Mottl, Department of Oceanography, University of Hawaii, 1000 Pope Road, Honolulu, HI 96822, USA. (mmottl@soest.hawaii.edu)

V. Spieß and L. Zühlsdorff, Department of Geosciences, University of Bremen, Fachbereich 5, Klagenfurterstrasse, Bremen, D-28203 Germany. (vspiess@uni-bremen.de; lzuehls@mtu.uni-bremen.de)

G. A. Spinelli, Earth and Environmental Science Department, New Mexico Institute of Mining and Technology, Socorro, NM 87801, USA. (spinelli@ees.nmt.edu)

C. G. Wheat, Global Undersea Research Unit, University of Alaska Fairbanks, P.O. Box 757220, Fairbanks, AK 99775, USA. (wheat@mbari.org)